IEEE *Access*
Multidisciplinary : Rapid Review : Open Access Journal

Mutually Injection Locked Multi-Element Terahertz Oscillator Based on AlGaN/GaN High Electron Mobility Avalanche Transit Time Devices

Partha Banerjee[1], Aritra Acharyya[2], Rajib Das[3], Arindam Biswas[4*], A. K. Bhattacharjee[5], Saurav Mallik[6], Haya Mesfer Alshahrani[7], E.ELSHIEKH[8], Mohamed Abbas[9] and Ben Othman Soufiene[10,*]

[1]Department of Electronics and Communication Engineering, Academy of Technology, Adisaptagram, Hooghly, West Bengal – 712121, India (E-Mail ID: parthabanerjee21@gmail.com)

[2]Department of Electronics and Communication Engineering, Cooch Behar Government Engineering College, Village: Harinchawra, P.O.: Ghughumari, Cooch Behar, West Bengal – 736170, India (Email ID: ari_besu@yahoo.co.in)

[3]Department of Electronics and Communication Engineering, Cooch Behar Government Engineering College, Village: Harinchawra, P.O.: Ghughumari, Cooch Behar, West Bengal – 736170, India (Email ID:)

[4]Centre for IoT and AI Integration with Education-Industry-Agriculture, Department of Mining Engineering, Kazi Nazrul University, Asansol, Burdwan 713340, West Bengal, India (E-Mail ID: mailarindambiswas@yahoo.co.in)

[5]Department of Electronics and Communication Engineering, National Institute of Technology, Durgapur, West Bengal – 713209, India (E-Mail ID: akbece12@yahoo.com)

[6]Department of Environmental Health, Harvard T H Chan School of Public Health, Boston, MA 02115, USA (email: sauravmtech2@gmail.com, smallik@hsph.harvard.edu)

[7]Department of Information Systems, College of Computer and Information Sciences, Princess Nourah bint Abdulrahman University, P.O.Box 84428, Riyadh, 11671, Saudi Arabia, hmalshahrani@pnu.edu.sa

[8]Department of Radiological Sciences, College of Applied medical Sciences, King Khalid University, Abha, Saudi Arabia. eelshiekh@kku.edu.sa

[9]Electrical Engineering Department, College of Engineering, King Khalid University, Abha 61421, Saudi Arabia; mabas@kku.edu.sa

[10]PRINCE Laboratory Research, ISITcom, Hammam Sousse, University of Sousse, Sousse, Tunisia.
*Correspondence: Ben Othman Soufiene (soufiene.benothman@isim.rnu.tn)

ABSTRACT The paper investigates the terahertz performance of a mutually injection-locked multi-element high electron mobility avalanche transit time (HEM-ATT) source based on AlGaN/GaN two-dimensional electron gas (2-DEG). Utilizing a nanostrip patch type planar coupling circuit, mutual injection locking between adjacent elements is achieved. The paper provides a comprehensive analysis of the integrated power combining technique in the mutually injection-locked multi-element HEM-ATT oscillator. A ten-element mutually injection-locked integrated power combined source is designed for operation at 1.0 THz, and simulation studies are conducted to examine its DC, large-signal, and avalanche noise characteristics. The capability of generating a narrow-band terahertz wave is verified by introducing various levels of structural mismatches between the elements. Results indicate that the ten-element HEM-ATT oscillator can deliver 2.27 W peak power with a 17% DC to THz conversion efficiency at 1.0 THz. The average noise measure of the oscillator is found to be 12.54 dB. Additionally, the terahertz performance of the mutually injection-locked ten-element HEM-ATT oscillator is compared with other state-of-the-art THz sources to evaluate its potentiality as an excellent integrated THz radiator.

INDEX TERMS 2-DEG, AlGaN/GaN, coupling circuit, HEM-ATT, injection locking, monolithic integration, power combination, terahertz.

I. INTRODUCTION

The terahertz (THz)-gap (0.3 – 10.0 THz), which is a significant portion of the THz frequency range has attracted considerable attention in the past few decades due to its extensive potential applications in various fields such as pharmaceuticals, biomedical engineering, industrial quality inspection, wireless communication, and more [1-15]. Recently, Quantum Cascade Lasers (QCLs) have addressed the upper part of the THz spectrum, providing coherent, high-power light waves at room temperature [16-19]. Concurrently, on the lower frequency side, solid-state electron devices operating at room temperature, including Resonant Tunneling Diodes (RTDs), Heterojunction Bipolar Transistors (HBTs), High Electron Mobility Transistors (HEMTs), and have emerged to fill this technological gap [20-29]. However, these devices suffer from limited radiated power (a few microwatts), disqualifying them for many THz applications. To overcome this limitation, power combination through array configurations of these devices has been explored. However, achieving constructive and sustained power combination requires mutual injection locking between oscillation elements, demanding synchronized frequency and stable phase relations [30-32]. Injection locking is a technique where an oscillator's frequency is stabilized by an external signal [33]. Since its application to IMPATT (Impact Avalanche and Transit Time) oscillators, this method has undergone significant advancements. Injection locking has evolved significantly since its inception in the early 20th century, transforming IMPATT oscillators from noisy, unstable devices to precise, reliable frequency sources. Numerous theoretical studies and experimental demonstrations of injection locking of solid-state oscillators were reported from the late 1960s to the mid-1970s [34-36]. In 1977, Okamoto *et al*. experimentally demonstrated a novel method of injection locking, using a low-frequency injection signal to lock a high-frequency solid-state oscillator [37]. Their method proved more effective in achieving a significantly wider locking bandwidth compared to the conventional subharmonic injection locking method. In 1978, Forrest *et al*. developed a large-signal theory of optical injection locking in IMPATT oscillators [38]. The 1980s saw significant research efforts focused on injection locking of solid-state oscillators [39, 40]. In 1991, Elad *et al*. reported a significant work on injection locking of IMPATT oscillators, where they

experimentally demonstrated a W-band (75 – 110 GHz) pulsed IMPATT oscillator injection locked to a continuous wave GUNN oscillator, achieving a high-power source with reasonably low noise in the millimeter-wave (mm-wave) frequencies [41]. Due to its extensive use in stabilizing low-noise solid-state oscillators operating in microwave, mm-wave, and THz regimes, injection locking of solid-state oscillators continues to attract research attention till date [42-45].

Within the realm of solid-state THz sources, impact avalanche transit time (IMPATT) diodes, utilizing wide-bandgap materials such as SiC and GaN, have demonstrated notable prowess in terms of high THz power delivery and efficient DC to THz conversion [46,47]. The GaN, owing to its exceptional thermal and electronic characteristics, stands out as particularly well-suited for the development of high-power and high-efficiency THz IMPATT sources. Nevertheless, the conventional vertical IMPATT structures (single-drift (SD) and double-drift (DD) region structures) face a noteworthy obstacle due to the elevated contact resistivity of the metal~p^+-GaN ohmic contact, thereby imposing limitations on their performance within the THz frequency range [48,49]. The edge-terminated reverse IMPATT structure and Schottky barrier IMPATT structure have been proposed as alternatives, with the latter recommended to avoid parasitic effects [50, 51]. The integration of HEMT structures based on AlGaN/GaN 2D-electron Gas (2-DEG) with Schottky barrier avalanche transit time (ATT) structures has been explored to leverage the THz potentialities of both structures [52]. Recent work by Khan *et al*. demonstrated a quasi-Read Schottky barrier lateral HEM-ATT structure capable of generating 1.0 THz frequencies [53]. This lateral orientation offers advantages in terms of monolithic integration using complementary metal–insulator–semiconductor (CMOS) technology. The suggested HEM-ATT configuration demonstrates enhanced THz power output and efficiency in contrast to regular THz DDR IMPATT structures. Through the lateral integration of numerous HEM-ATT diodes, it becomes feasible to establish an oscillator array on a monolithic integrated circuit, thereby creating a broadband THz source. Furthermore, the inclusion of a third terminal (gate) positioned over the AlGaN layer facilitates direct modulation of power and frequency by an externally applied signal, imparting versatility to the structure for a range of applications.

A notable development is the power-combined Graphene Nanoribbon (GNR) based IMPATT oscillator proposed by A. Acharyya in 2020, achieving high-power delivery in the order of milli-watts at 1.0 THz [54]. In this context, our paper introduces a mutually injection locked multi-element HEM-ATT source, connecting the HEM-ATT elements parallelly in power-combined mode. Recognizing the challenges of fabricating exactly identical diodes, mutual injection locking is proposed via a planar circuit-based coupling between successive elements. This paper presents an analysis of the suggested mutual injection-locked multi-element HEM-ATT source, starting with a two-element coupled oscillator analysis. The subsequent sections extend this analysis to coupled multi-element oscillators, considering structural mismatches between the elements. Conducting simulations and comparing the results with both simulation and experimental data from various THz IMPATT sources validate the superior performance of the proposed source, particularly within the THz frequency bands.

II. STRUCTURE AND FABRICATION

The mutually injection locked multi-element HEM-ATT source structure is characterized by its intricate design, as depicted in Figures 1(a) and 1(b) for the cross-sectional front view and top view, respectively. These figures illustrate a six-element HEM-ATT structure due to space constraints in the enlarged views. However, it's crucial to note that the final design and investigations are conducted for a ten-element HEM-ATT structure, as detailed in Table 1. To achieve the desired material properties, the mole fraction of aluminum (Al) in the $Al_xGa_{1-x}N$ layers is set to $x = 0.2$. The fabrication process begins with a 400 nm thick, double-side polished n-GaN substrate with a diameter of 4 inches. The high-temperature metal-organic chemical vapour deposition (MOCVD) technique can be employed to grow the device structure on the n-GaN substrate with a doping concentration of 10^{23} m^{-3}. The growth sequence starts with a 350 nm thick undoped GaN buffer layer at 1300°C, followed by a temperature reduction to 1180°C for the deposition of a 20 nm thick unintentionally doped $Al_{0.2}Ga_{0.8}N$ barrier layer. Then a Si_3N_4 hard mask layer must be grown on the top layer using plasma-enhanced chemical vapour deposition (PECVD). The device patterns can be transferred to the mask layer through standard photolithography and reactive ion etching (RIE) processes. Subsequently, the fabrication process involves a series of steps, including the etching of trenches on the $Al_{0.2}Ga_{0.8}N$ barrier layer, the deposition of an n^+-GaN cathode contact layer (Si dosage: 2.0×10^{24} m^{-3}), and the deposition of

Schottky anode (Ni(30nm)/Au400(nm)), Ohmic cathode (Ti(30nm)/Au(200nm)), and coupling circuit (Al (100nm)). This process requires five successive Si_3N_4 hard masking, photolithography, and RIE steps. Then the wafer must be flipped, and a thermal evaporation process must deposit an $80 - 100$ nm thick layer of aluminum to prepare the ground plane. The implementation of a Cu-based vertical interconnect is required between the ground plane and anode. This can be achieved through copper-filled interchip vias using Cu-CVD, following the MOCVD TiN diffusion barrier process detailed in ref. [55]. The proposed structure can be successfully fabricated using the outlined process flow, providing a foundation for the realization of a mutually injection locked multi-element HEM-ATT oscillator.

III. MODELLING AND SIMULATION OF DEVICE AND COUPLING CIRCUIT

The Silvaco-ATLAS platform was utilized to perform steady-state DC simulations of a single HEM-ATT device [53]. To determine the steady-state output parameters of the HEM-ATT device at a specific current density, a time-independent Poisson equation, carrier continuity equations, and current density equations were solved, accounting for appropriate boundary conditions. The simulations assumed that the device's junction temperature equaled the ambient temperature (300 K). The 2-DEG electron density was determined by utilizing information about the sheet charge density induced from polarization [56]. In the computation of the polarization-induced 2-DEG electron density, the influence of AlGaN/GaN interface charges was taken into account. The maximum sheet carrier density at the undoped AlGaN/GaN interface is articulated as follows:

$$n_s(x) = \frac{+\sigma(x)}{q} - \left(\frac{\epsilon_0\epsilon_r(x)}{h_aq^2}\right)[q\Phi_b(x) + E_F(x) - \Delta E_c(x)], \quad (1)$$

where h_a signifies the AlGaN layer thickness, σ represents the concentration of sheet charge induced through polarization, $\epsilon_r(x)$ denotes spatially varying relative permittivity, ϵ_0 is the permittivity in vacuum (8.854×10^{-12} F m^{-1}), q is the electron charge (1.6×10^{-19} C), E_F is the Fermi level, ΔE is the conduction-band offset, and $q\Phi_b$ is the Schottky barrier. The thickness of the AlGaN layer significantly influences the local maximum sheet carrier density at the AlGaN/GaN interface [57-59]. HEM-ATT devices illustrated in Figure 1 (a) exhibit classical SDR density profiles in 2-DEG channel due to trenches at two positions: trench – 1 at the cathode-side and trench – 2 at the anode-side [53]. Figure 2 (a) depicts a low-high-low (lo-hi-lo) 2-D model for simulating the lo-hi-lo HEM-ATT

structure, with regions 1, 2, 3, and 4 corresponding to the GaN buffer, AlGaN barrier layers, Si_3N_4 passivation layer associated with the anode-side, and cathode-side, respectively.

After a successful steady-state (DC) simulation at a specific current density value (J_0), the resulting DC parameters, including avalanche width, drift width, avalanche voltage, drift voltage, breakdown voltage, etc., were extracted and recorded. These DC parameters served as initial conditions for subsequent large-signal simulations at the same J_0 value. A non-sinusoidal-voltage-excited (NSVE) large-signal (L-S) model, detailed in reference [60], was utilized for the large-signal simulation. Outcomes of the L-S analysis corresponding to the given J_0 were pulled out and kept. Key L-S parameters included time-domain voltage and current waveforms, frequency domain representations of those, and additional metrics like diode impedance, resistance, reactance, and parasitic series resistance, all expressed as functions of frequency (f) and J_0. Subsequently, the J_0 value was updated, initiating an iterative process that continued until the steady-state analysis failed to converge. This iterative approach was employed to comprehensively characterize the complete THz performance of the diode structure across the full frequency spectrum [53].

The coupling circuits can be established through planar nanostrip lines. Each nanostrip facilitates a coupling between the cathode-side edge of one diode and the anode-side edge of the next diode. The dimensions of the coupling circuit components (L_{C1}, L_{C2}, S_{C1}, S_{C2}, W_{C1}, W_{C2}, T_{C1}, T_{C2}, d_{C1}, d_{C2}, g_{C1}, and g_{C2}), illustrated in Figures 1 (a) and (b), need careful design. They should enable a portion of the induced high-frequency current from the cathode-side of the first diode to seamlessly transfer to the anode-side of the second diode via the coupling circuit, maintaining the current's phase angle. This coupling process extends from the second diode to the third diode, and so forth. The nanostrip line's ground plane must be connected to the common anode through the vertical interconnection, as depicted in Figure 1 (a). The design and extraction of values for the equivalent RLC model parameters in the coupling circuits were executed using Advanced Designing System (ADS) software. Figure 2 (b) illustrates the external high-frequency equivalent circuit model of the mutually injection locked N-element HEM-ATT source operating under free oscillating conditions. In this representation, $Z_C^{(i,i+1)}$ for all i from 1 to $(N-1)$ signifies the equivalent impedance of the coupling circuit between the ith and $(i+1)$[th] diodes. Here, I_0 denotes the total bias current, and $v_{THz}(t)$ acts as a voltage source connected in parallel to the

oscillator through capacitive coupling. This voltage source represents the THz voltage across the diodes during stable oscillation.

It is evident that the HEM-ATT diodes cannot be entirely identical, as some degree of mismatch in either dimension or doping is inherent. Consequently, the breakdown voltages of different HEM-ATTs are expected to vary slightly. However, the parallel operation of these diodes remains unaffected by the mismatch in breakdown voltage (V_B). The V_B exhibits a positive temperature coefficient. Consequently, during the initial moments of oscillation, the diode with the lowest V_B dissipates all the power. This leads to the heating of that diode, causing an increase in its V_B, enabling the next diode to break down, and so forth. The transient period, spanning a duration of a few nanoseconds (ns), concludes as all diodes undergo breakdown, leading to a distinctive voltage drop across the parallel system in the state of stable oscillation [61].

The overall oscillator circuit's equivalent circuit is depicted in Figure 2 (c). The impedance of the ith diode ($Z_d^{(i)}, i \in \{1,2,3,\ldots,(N-1)\}$) can be derived from 1-D self-consistent quantum drift-diffusion (SCQDD) simulations as previously documented [62, 63]. This diode impedance can be decomposed into resistance ($R_d^{(i)}$) and reactance ($X_d^{(i)}$), both highly dependent on the J_0. The diode impedance is divided into M segments linked in series ($Z_{d(k)}^{(i)} = R_{d(k)}^{(i)} - X_{d(k)}^{(i)}$; $i \in \{1,2,3,\ldots,N\}, k \in \{1,2,3,\ldots,M\}$). Utilizing SCQDD simulation [49], the spatial distributions of negative resistance and capacitive reactance per unit length for a specific diode can be determined. In Figure 2 (d), a schematic is presented to illustrate the calculation approach for the impedance of a typical diode (such as HEM-ATT (1)), based on the spatial distributions of diode resistance and reactance per unit length (i.e. $\mathfrak{R}_d^{(1)}(x)$ vs. x and $\aleph_d^{(1)}(x)$ vs. x) for $M = 3$. The entire active region of the diode (L_d) is partitioned into three equal regions (from $x = x_{(1)}$ to $x = x_{(2)}$, from $x = x_{(2)}$ to $x = x_{(3)}$ and from $x = x_{(3)}$ to $x = x_{(4)}$). The negative resistance and capacitive reactance of the ith diode's k[th] active region are calculated as follows:

$$R_{d(k)}^{(i)} = \int_{x=x_{(k)}}^{x=x_{(k+1)}} \mathfrak{R}_d^{(i)}(x)dx, \text{ and } X_{d(k)}^{(i)} = \int_{x=x_{(k)}}^{x=x_{(k+1)}} \aleph_d^{(i)}(x)dx. \quad \text{(2 (a) \& (b))}$$

The cathode-side series resistance ($R_C^{(i)}$) due to un-swept depletion layer, n^+-GaN layer, and n^+-GaN~metal ohmic contact resistance, along with the anode-side series resistance ($R_A^{(i)}$) due to the Schottky barrier, are computed using a L-S simulation technique based on depletion width

modulation phenomena under oscillating conditions [60]. Shunt capacitances $(C_{a(i)}^{(1)} = \Delta Q^{(i)}/\Delta V^{(i)}, i = 1, 2,$ and $3)$ are determined from the electric charge and potential distributions along the active region obtained through SCQDD simulation [62]. These computations can be expanded for M values greater than three (3), ensuring a high degree of precision. Following this, the equivalent coupling circuit parameters, including series capacitances $((C_{C(K)}^{(i,i+1)}, C_{C(A)}^{(i,i+1)})$, series inductance $(L^{(i,i+1)})$, series resistance $(R_L^{(i,i+1)})$,), and shunt capacitances $(C_{Ca(k)}^{(i,i+1)}, k = 1, 2,$ and $3)$ between the ith and $(i + 1)^{\text{th}}$ diodes (for i values from 1 to N), are derived from simulations in the ADS software, as previously mentioned. Table 1 furnishes a comprehensive compilation of all the design parameters for the 1.0 THz mutually coupled ten-element HEM-ATT source.

IV. MUTUALLY INJECTION LOCKED N-ELEMENT HEM-ATT OSCILLATOR

Before delving into the analysis of the mutually injection locked multi-element (N-number of HEM-ATTs) HEM-ATT oscillator, it is essential to consider the mutual coupling between two HEM-ATT sources. The reduced equivalent circuit of the 2-element oscillator is depicted in Figure 3 (a). For simplicity, shunt capacitances $(C_{ca(1)}^{(1,2)}, C_{ca(2)}^{(1,2)},$ and $C_{ca(3)}^{(1,2)})$ associated with the coupling circuit are neglected due to the substantial thickness of the insulating layer between the coupling circuit and the ground plane $((t_{OX} + t_{buff}) > 0.4$ μm). The equivalent circuit of HEM-ATT (1) comprises four main elements:

(i) Anode contact resistance $(R_A^{(1)})$ due to the Schottky barrier.

(ii) Cathode-side parasitic series resistance $(R_C^{(1)})$ arising from the un-swept depletion layer, n^+-GaN layer, and n^+-GaN~metal ohmic contact resistance.

(iii) Series impedance components related to the device's active layer $(Z_{d(i)}^{(1)} = R_{d(i)}^{(1)} - X_{d(i)}^{(1)}$, where $X_{d(i)}^{(1)} = j/\omega C_{d(i)}^{(1)}$, and $i \in \{1,2,3,\dots,M\}$.

(iv) Shunt capacitances associated with the device's active layer $(C_{a(i)}^{(1)}$, where $i = 1, 2, 3, \dots., M)$.

The $Z_{d(i)}^{(1)}$ and $C_{d(i)}^{(1)}$ are computed for three equal sections of the device's active layer using the high-frequency simulation method [62]. Increasing the value of 'M' introduces complexity in circuit analysis, but for $M = 3$, the change in $Z_{d(i)}^{(1)}$ and $C_{d(i)}^{(1)}$ remains within $1 - 3\%$. This

choice ($M = 3$) minimizes complexity without significantly affecting the accuracy of calculations. From Figure 3 (a), the equivalent impedance of HEM-ATT (1) without $R_C^{(1)}$ is derived as [54]:

$$Z_d^{(1)} = \left\{ \left(\frac{c_{a(2)}^{(1)} Z_{d(1)}^{(1)}}{j\omega c_{a(1)}^{(1)} c_{a(2)}^{(1)} Z_{d(1)}^{(1)} + c_{a(1)}^{(1)} + c_{a(2)}^{(1)}} \right) + \left[\frac{j\omega c_{a(3)}^{(1)} Z'_2 Z_3}{j\omega c_{a(3)}^{(1)} (Z'_2 + Z_3) + 1} \right] + \left[\frac{j\omega c_{a(4)}^{(1)} Z'_5 Z_6}{j\omega c_{a(4)}^{(1)} (Z'_5 + Z_6) + 1} \right] + \left(\frac{Z'_8 Z_9}{Z'_8 + Z_9} \right) \right\}, \quad (3)$$

where

$$Z'_2 = \left\{ \frac{\left(j\omega c_{a(1)}^{(1)} c_{a(2)}^{(1)} Z_{d(1)}^{(1)} + c_{a(1)}^{(1)} + c_{a(2)}^{(1)} \right) Z_{d(2)}^{(1)} + c_{a(2)}^{(1)} Z_{d(1)}^{(1)}}{\left(j\omega c_{a(1)}^{(1)} c_{a(2)}^{(1)} Z_{d(1)}^{(1)} + c_{a(1)}^{(1)} + c_{a(2)}^{(1)} \right)} \right\},$$

and $Z_3 = \left\{ \frac{1}{j\omega \left(j\omega c_{a(1)}^{(1)} c_{a(2)}^{(1)} Z_{d(1)}^{(1)} + c_{a(1)}^{(1)} + c_{a(2)}^{(1)} \right)} \right\}.$ (4 (a) & (b))

Expressions for Z_5, Z'_5, Z_8 and Z'_8 in equation (3) are obtained from:

$$Z_i = \left\{ \frac{Z'_{i-3}}{\left[j\omega C_{a\left(3+\left\{\frac{i-5}{3}\right\}\right)}^{(1)} (Z'_{i-3} + Z_{i-2}) + 1 \right]} \right\}, \quad \text{and} \quad Z'_i =$$

$$\left\{ \frac{\left[j\omega C_{a\left(3+\left\{\frac{i-5}{3}\right\}\right)}^{(1)} (Z'_{i-3} + Z_{i-2}) + 1 \right] Z_X^{(1)} + Z_i}{\left[j\omega C_{a\left(3+\left\{\frac{i-5}{3}\right\}\right)}^{(1)} (Z'_{i-3} + Z_{i-2}) + 1 \right]} \right\}, \quad (5 \text{ (a) \& (b)})$$

with $i = 5$ and 8, where $Z_X^{(1)} = Z_{d(3)}^{(1)}$ for $i = 5$ and $Z_X^{(1)} = R_A^{(1)}$ for $i = 8$. Similarly, Z_6 and Z_9 in equation (3) are obtained from:

$$Z_j = \left\{ \frac{z_{j-3}}{\left[j\omega C_{a\left(3+\left\{\frac{j-6}{3}\right\}\right)}^{(1)} (Z'_{j-4} + Z_{j-3}) + 1 \right]} \right\}, \text{for } j = 6 \quad \text{and}$$

$j = 9.$ (6)

Proceeding in the similar way, the equivalent impedance of the HEM-ATT (2), i.e. $Z_d^{(2)}$ without $R_A^{(2)}$ can be obtained. Once both $Z_d^{(1)}$ and $Z_d^{(2)}$ are obtained, those can be resolved into real negative resistance ($R_d^{(m)}$, where $m = 1, 2$) and imaginary capacitance ($C_d^{(m)}$, where $m = 1$ and 2); thus the equivalent impedance of HEM-ATT (m) can be expressed as $Z_d^{(m)} = R_d^{(m)} - j/\omega C_d^{(m)}$, where $m = 1$ and 2. Now the simplified equivalent circuit of the 2-element HEM-ATT oscillator involving $R_C^{(1)}, Z_d^{(1)}, Z_d^{(2)}, R_A^{(2)},$ and the coupling circuit comprises of series connected

IEEE *Access*

resistance $(R_L^{(1,2)})$, inductance $(L^{(1,2)})$ and capacitance $(C^{(1,2)} = C_{C(K)}^{(1,2)} C_{C(A)}^{(1,2)} / (C_{C(K)}^{(1,2)} + C_{C(A)}^{(1,2)}))$ is shown in Figure 3 (b). The 2-port model of the oscillator and its Z-parameter equivalent are depicted in Figures 3 (c) and (d). The said 2-port network consists of port: $1 - 1'$ and port: $2 - 2'$. The Z-parameters associated with the 2-port network can be expressed as:

$$Z_{11}(\omega) = \left(R_L^{(1,2)} + R_{s(p)}^{(2)}\right) + j\left(\omega L^{(1,2)} - \frac{1}{\omega C^{(1,2)}} - \frac{1}{\omega c_d^{(1)}}\right),$$
(7)

$$Z_{12}(\omega) = Z_{21}(\omega) = R_L^{(1,2)} + j\left(\omega L^{(1,2)} - \frac{1}{\omega C^{(1,2)}}\right),$$
(8)

$$Z_{22}(\omega) = \left(R_L^{(1,2)} + R_{s(n)}^{(1)}\right) + j\left(\omega L^{(1,2)} - \frac{1}{\omega C^{(1,2)}} - \frac{1}{\omega c_d^{(2)}}\right).$$
(9)

Due to the reciprocal nature of the two-port network, the transfer impedances are equal, i.e. $Z_{12}(\omega) = Z_{21}(\omega)$. Now, the matrix form of the two-port network equations in frequency-domain can be written as:

$$\begin{bmatrix} (Z_{11} - R_d^{(1)}) & Z_{12}(\omega) \\ Z_{12} & (Z_{22} - R_d^{(2)}) \end{bmatrix} \begin{bmatrix} I_1 \\ I_2 \end{bmatrix} = \begin{bmatrix} V_1 \\ V_2 \end{bmatrix},$$
(10 (a) & (b))

where the oscillation voltage at port $1 - 1'$ and port $2 - 2'$ are identical, i.e. $V_1(\omega) = V_2(\omega) = V_{THz}^{(1,2)}(\omega)$, which is the THz oscillating voltage across the two-element oscillator. If the HEM-ATT (1) is solely operated, i.e. when $I_2 = 0$, then equation (10 (a)) can be written as:

$$\left(R_L^{(1,2)} + R_A^{(2)} - R_d^{(1)}\right)I_1(\omega) + j\left(\omega^{(1)}L^{(1,2)} - \right.$$
$$\left. \frac{1}{\omega^{(1)}C^{(1,2)}} - \frac{1}{\omega^{(1)}c_d^{(1)}}\right)I_1(\omega) = V_{THz}^{(1)}(\omega),$$
(11)

where $\omega^{(1)}$ and $V_{THz}^{(1)}(\omega)$ are the oscillation frequency and voltage of the standalone HEM-ATT (1). Similarly, if the HEM-ATT (2) is solely operated, i.e. when $I_1 = 0$, then equation (10 (b)) can be written as:

$$\left(R_L^{(1,2)} + R_C^{(1)} - R_d^{(2)}\right)I_2(\omega) + j\left(\omega^{(2)}L^{(1,2)} - \right.$$
$$\left. \frac{1}{\omega^{(2)}C^{(1,2)}} - \frac{1}{\omega^{(2)}c_d^{(2)}}\right)I_2(\omega) = V_{THz}^{(2)}(\omega),$$
(12)

where $\omega^{(2)}$ and $V_{THz}^{(2)}(\omega)$ are the oscillation frequency and voltage of the standalone HEM-ATT (2). The imaginary

parts of the left-hand and right-hand sides of the equations (11) and (12) can be equated to obtain $\omega^{(1)}$ and $\omega^{(2)}$ respectively. Those are given by:

$$\omega^{(m)} = \left(\frac{C^{(1,2)} + c_d^{(m)}}{L^{(1,2)} C^{(1,2)} c_d^{(m)}}\right)^{\frac{1}{2}},$$
(13 (a) & (b))

where $m = 1, 2$. Now, the transformation of equations (11) and (12) into time-domain from frequency-domain can be obtained by substituting $j\omega I_m(\omega) \equiv di_m(t)/dt$ and $V_{THz}^{(m)}(\omega) \equiv v_{THz}^{(m)}(t)$, where $m = 1$ and 2. The matrix form of those time-domain equations can be written as:

$$\begin{bmatrix} (R_L^{(1,2)} + R_A^{(2)} - R_d^{(1)}) & \left(L^{(1,2)} - \frac{1}{\omega^2 C^{(1,2)}} - \frac{1}{\omega^2 c_d^{(1)}}\right) \\ (R_L^{(1,2)} + R_C^{(1)} - R_d^{(2)}) & \left(L^{(1,2)} - \frac{1}{\omega^2 C^{(1,2)}} - \frac{1}{\omega^2 c_d^{(2)}}\right) \end{bmatrix} \begin{bmatrix} \frac{di_1(t)}{dt} \\ \frac{di_2(t)}{dt} \end{bmatrix} = \begin{bmatrix} v_{rf}^{(1)}(t) \\ v_{rf}^{(2)}(t) \end{bmatrix},$$
(14 (a) & (b))

where for $m = 1$ and 2, oscillation voltage for each standalone oscillator can be expressed as a no-sinusoidal voltage form given by [60]:

$$v_{rf}^{(m)}(t) = V_B^{(m)} \sum_{s=1}^{r} (m_x)^r \sin(s\omega t),$$
(15)

where m_x is the voltage modulation index and $V_B^{(m)}$ are the DC voltage drop across individual standalone oscillators ($s = 1$ corresponds to the fundamental frequency of oscillation, and $s = r$ is corresponding to the rth harmonic component) [60]. The numerical solutions to the differential equations presented in equations (14 (a) & (b)) yield the time-domain currents ($i_1(t)$ and $i_2(t)$) for the individual standalone oscillators. Due to the adoption of a numerical approach, the continuous-time current signal ($i_m(t)$, where $m \in \{1,2\}$ and $t \in (0, \infty)$), is subsequently discretized into a discrete-time signal $i_m(t)$, where $k \in \{1,2,3, \dots (U-1)\}$ (considering U as the count of time instances under consideration). Consequently, the THz power radiated by the standalone HEM-ATT (m) can be determined using the following expression:

$$P_{THz}^{(m)} = \left|R_d^{(m)}\right| \lim_{U \to \infty} \left(\frac{1}{U}\right) \sum_{k=0}^{U-1} |i_m(k)|^2,$$
(16)

where $m = 1, 2$. If HEM-ATT (1) and HEM-ATT (2) operate concurrently, the voltage drop across them will be identical. This similarity arises from the earlier discussion and is attributed to their parallel operation. Consequently, equations (10 (a) & (b)) are simplified into the ensuing matrix form:

$$\begin{bmatrix} \begin{cases} \left(R_L^{(1,2)} + R_A^{(2)} - R_d^{(1)}\right) \\ +j\left(\omega L^{(1,2)} - \frac{1}{\omega C^{(1,2)}} - \frac{1}{\omega C_d^{(1)}}\right) \end{cases} & \left\{R_L^{(1,2)} + j\left(\omega L^{(1,2)} - \frac{1}{\omega C^{(1,2)}}\right)\right\} \\ \left\{R_L^{(1,2)} + j\left(\omega L^{(1,2)} - \frac{1}{\omega C^{(1,2)}}\right)\right\} & \begin{cases} \left(R_L^{(1,2)} + R_C^{(1)} - R_d^{(2)}\right) \\ +j\left(\omega L^{(1,2)} - \frac{1}{\omega C^{(1,2)}} - \frac{1}{\omega C_d^{(2)}}\right) \end{cases} \end{bmatrix} \begin{bmatrix} I_1 \\ I_2 \end{bmatrix} = \begin{bmatrix} V_{THz}^{(1,2)}(\omega) \\ V_{THz}^{(1,2)}(\omega) \end{bmatrix}.$$

(17 (a) & (b))

The oscillation frequency of the 2-element oscillator can be obtained by equating the imaginary part of the coefficient determinant of equations (17 (a) & (b)) to zero, i.e. $Imag(\Delta_Z) = 0$. Therefore, under the mutually injection locked oscillation condition, the oscillation frequency of the two-element oscillator can be obtained as:

$$\omega^{(1,2)} =$$
$$\begin{cases} \frac{\frac{1}{C_d^{(1)}}\left(R_C^{(1)} - R_d^{(1)}\right) + \frac{1}{C_d^{(2)}}\left(R_A^{(2)} - R_d^{(2)}\right) + R_L^{(1,2)}\left(\frac{1}{C_d^{(1)}} + \frac{1}{C_d^{(2)}}\right)}{L^{(1,2)}\left(R_C^{(1)} + R_A^{(2)} - R_d^{(1)} - R_d^{(2)}\right)} - \\ \left(\frac{1}{L^{(1,2)}C^{(1,2)}}\right) \end{cases}.$$

(18)

By transforming equations (17 (a) & (b)) into time-domain, the following two differential equations can be obtained:

$$A_1 \frac{di_1(t)}{dt} + B_1 i_1(t) + D_1 \frac{di_2(t)}{dt} + E_1 i_2(t) = V_1,$$ (19)

$$A_2 \frac{di_2(t)}{dt} + B_2 i_2(t) + D_2 \frac{di_1(t)}{dt} + E_2 i_1(t) = V_2,$$ (20)

where

$$A_1 = \left(L^{(1,2)} - \frac{1}{\omega^2 C^{(1,2)}} - \frac{1}{\omega^2 C_d^{(1)}}\right), A_2$$
$$= \left(L^{(1,2)} - \frac{1}{\omega^2 C^{(1,2)}} - \frac{1}{\omega^2 C_d^{(2)}}\right),$$

$$B_1 = \left(R_L^{(1,2)} + R_{s(p)}^{(2)} - R_d^{(1)}\right), B_2$$
$$= \left(R_L^{(1,2)} + R_{s(n)}^{(1)} - R_d^{(2)}\right), D_1 = D_2$$
$$= \left(L^{(1,2)} - \frac{1}{\omega^2 C^{(1,2)}}\right),$$

$$E_1 = E_2 = R_L^{(1,2)}, \text{and } V_1 = V_2 = V_B \sum_{s=1}^{r}(m_x)^r \sin(s\omega t).$$

Employing the Runge-Kutta technique to simultaneously solve the two aforementioned differential equations yields discrete solutions for $i_1(k)$ and $i_2(k)$, where $k = 0, 1, 2, 3, \ldots, (U - 1)$. Consequently, the overall THz power emitted by the mutually synchronized HEM-ATT (1) and HEM-ATT (2) sources can be determined from:

$$P_{THz}^{(1,2)} = \sum_{m=1}^{2}\left[|R_d^{(m)}|\lim_{U\to\infty}\left(\frac{1}{U}\right)\sum_{k=0}^{U-1}|i_m(k)|^2\right].$$ (21)

Following the derivation of the fundamental time-domain equations for the 2-element oscillator (specifically, equations (19), (20)), the foundational time-domain equations for a multi-element injection locked oscillator can be established. Extending from equations (19) and (20) designed for the 2-element injection locked oscillator, the fundamental equations for an N-element coupled oscillator system can be formulated as:

$$diag(A_1, A_2, \ldots, A_N)\frac{d|i\rangle}{dt} + diag(B_1, B, \ldots, B_N)|i\rangle + D\frac{d|i\rangle}{dt} + E|i\rangle = |V\rangle,$$ (22)

where

$$|i\rangle = \begin{pmatrix} i_1(t) \\ i_2(t) \\ i_3(t) \\ \vdots \\ i_N(t) \end{pmatrix}, |V\rangle = \begin{pmatrix} V_1 \\ V_2 \\ V_3 \\ \vdots \\ V_N \end{pmatrix},$$

$$V_i = V_B \sum_{s=1}^{r}(m_x)^r \sin(s\omega t) \, \forall i \in [1, N],$$

$$diag(A_1, A_2, \ldots, A_N) = \begin{pmatrix} A_1 & 0 & 0 & \ldots & 0 \\ 0 & A_2 & 0 & \ldots & 0 \\ 0 & 0 & A_3 & \ldots & 0 \\ \ldots & \ldots & \ldots & \ldots & \ldots \\ 0 & \ldots & \ldots & 0 & A_N \end{pmatrix},$$

$$diag(B_1, B, \ldots, B_N) = \begin{pmatrix} B_1 & 0 & 0 & \ldots & 0 \\ 0 & B_2 & 0 & \ldots & 0 \\ 0 & 0 & B_3 & \ldots & 0 \\ \ldots & \ldots & \ldots & \ldots & \ldots \\ 0 & \ldots & \ldots & 0 & B_N \end{pmatrix},$$

$$D = \begin{pmatrix} 0 & \left(L^{(1,2)} - \frac{1}{\omega^2 C^{(1,2)}}\right) & 0 & \ldots & 0 \\ \left(L^{(1,2)} - \frac{1}{\omega^2 C^{(1,2)}}\right) & 0 & \left(L^{(2,3)} - \frac{1}{\omega^2 C^{(2,3)}}\right) & \ldots & 0 \\ 0 & L^{(2,3)} - \frac{1}{\omega^2 C^{(2,3)}} & 0 & \ldots & 0 \\ \ldots & \ldots & \ldots & \ldots & \ldots \\ 0 & \ldots & \ldots & L^{(N-1,N)} - \frac{1}{\omega^2 C^{(N-1,N)}} & 0 \end{pmatrix},$$

$$E = \begin{pmatrix} 0 & R_L^{(1,2)} & 0 & \ldots & 0 \\ R_L^{(1,2)} & 0 & R_L^{(2,3)} & \ldots & 0 \\ 0 & R_L^{(3,2)} & 0 & \ldots & 0 \\ \ldots & \ldots & \ldots & \ldots & \ldots \\ 0 & \ldots & \ldots & R_L^{(N-1,N)} & 0 \end{pmatrix}.$$

Therefore, the magnitude and phase of the coupling parameters between two consecutive elements (specifically, between the ith and $(i + 1)$[th] elements, where $i \in \{1,2,3, \ldots, (N - 1)\}$) are determined as follows:

$$\left|\kappa^{(i,i+1)}\right| = \left\{ \left(R_L^{(i,i+1)}\right)^2 + \left(\omega L^{(i,i+1)} - \right.\right.$$

$$\left.\left.\frac{1}{\omega C^{(i,i+1)}}\right)^2 \right\}^{\frac{1}{2}}, \text{and } \angle\kappa^{(i,i+1)} = tan^{-1}\left\{\frac{\left(\omega L^{(i,i+1)} - \frac{1}{\omega C^{(i,i+1)}}\right)}{R_L^{(i,i+1)}}\right\}.$$

(23)

Subsequently, by employing the Runge-Kutta technique to simultaneously solve the aforementioned set of N differential equations described in equation (22), discrete solutions for $i_k(n)$ where $k \in \{1,2,3,...,N\}$ are obtained. Consequently, the power emitted by the mutually coupled N-element HEM-ATT source can be expresses as:

$$P_{THz} = \sum_{m=1}^{N}\left[\left|R_d^{(w)}\right|\lim_{U\to\infty}\left(\frac{1}{U}\right)\sum_{k=0}^{U-1}|i_m(k)|^2\right].$$ (24)

V. MODELLING AND SIMULATION OF NOISE

The stochastic impact ionization process in an IMPATT device introduces unwanted fluctuations in current and field within its steady-state constituents. These variations present themselves as small-signal components in proportion to their steady-state values during reverse bias breakdown conditions. Therefore, to accurately simulate noise in a mutually injection locked multi-element HEM-ATT source, it is essential to perform the simulation under small-signal conditions. Figure 4 illustrates the equivalent circuit for avalanche noise simulation, where noise sources $v_n^{(i)}, i \in \{1,2,3,...,N\}$, replace diode impedances. Given the parallel arrangement of these noise sources, the equivalent noise voltage is articulated as $v_{n(eqvt)} = v_n^{(1)} = v_n^{(2)} = \cdots = v_n^{(N)}$. Small-signal avalanche noise simulation is executed under open-circuit conditions, devoid of any applied high-frequency AC voltage signal [64]. The simulation employs two 2nd-order differential equations, corresponding to the real and imaginary components of the equivalent noise field. These equations are simultaneously solved using the Runge–Kutta method, with band-to-band tunneling considered as a noiseless instantaneous process [65]. This simulation approach, known as the double-iterative field-maximum (DIFM) method [64, 65], is utilized. Subsequently, the transfer noise impedance at each spatial point of the depletion layer is computed based on the knowledge of mean square noise current and voltage. Furthermore, the mean square noise equivalent voltage $\langle v_{n(eqvt)}^2\rangle$ is derived from the distribution of transfer noise impedance along the depletion layer. This allows for the determination of the noise spectral density (NSD(f) = $\langle v_{n(eqvt)}^2\rangle/df$ V^2 s) or mean square noise voltage per bandwidth (df) as a function of f. To assess the noise

performance of the source, the noise measure (NM) is calculated and defined as:

$$\text{NM}(f) = \frac{\text{NSD}(f)}{4k_BT(-R_{d(eqvt)}(f) - R_{s(eqvt)})},$$ (25)

where $k_B = 1.38 \times 10^{-23}$ J K^{-1} is the Boltzmann constant, $T = 300$ K is the ambient temperature, $R_{d(eqvt)}(f)$ is the equivalent negative resistance, and $R_{s(eqvt)}$ is the equivalent series resistance of the parallel-connected N-element HEM-ATTs.

VI. RESULTS AND DISCUSSION

In this section, we begin by presenting the steady-state characteristics of the 10-element HEM-ATT structure derived from the Silvaco ATLAS simulation platform. Following that, we delve into the description of the coupling circuits designed for the structure, elucidating their characteristics based on simulations conducted in ADS software. Subsequently, we explore the THz performance of the 10-element HEM-ATT source with mutual injection locking as well as the avalanche noise characteristics of the source under examination. Finally, the performance of the ten-element 1.0 THz HEM-ATT oscillator under mutual injection locking has been compared with that of several state-of-the-art THz sources.

A. STEADY-STATE CHARACTERISTICS

The Silvaco ATLAS platform played a crucial role in conducting a steady-state analysis of the multi-element HEM-ATT structure. The analysis employed a modified drift–diffusion model, encompassing the Poisson equation, carrier continuity equation, and current density equation. Several factors were taken into consideration during the simulation, including concentration and field-dependent mobility (conmob and fldmob), Shockley–Read–Hall and Auger recombinations (srh and auger), band-to-band tunneling (autobbt), trap-assisted tunneling, and more. Additionally, the simulation model accounted for Fermi statistics (fermi) and the effects of bandgap narrowing (bgn), interface charges, charge trapping, passivation, mobile space charge, etc. Before initiating the static simulation of the proposed structure, the entire simulation model underwent calibration against experimental data obtained from previously published reports [66, 67]. The quasi-Read concentration profile of the proposed multi-element HEM-ATT structure, characterized by a lo-hi-lo pattern, was verified by analyzing the partial electron distribution at the AlGaN/GaN interfaces (at $y = h_g$ for $(L_{Au(Sch)} + L_{Ni(Sch)} \leq x \leq (L_d + L_{Au(Sch)} + L_{Ni(Sch)}))$). This distribution is influenced by the polarization-induced sheet

charges in the channel region. The partial electron density beneath the 20 nm thick AlGaN barrier layer was determined to be 3.4527×10^{23} m^{-3}, representing the high (hi) electron density regions. Similarly, the partial electron density beneath the 10 nm thick trench regions was measured at 6.2398×10^{22} m^{-3}, indicating the low (lo) electron density regions. Consequently, adjusting the thickness of the AlGaN barrier layer allows for the modification of the concentration profile in the channel region, and this property was utilized to achieve a quasi-Read density profile in the proposed structure.

The characterization of the ten-element HEM-ATT structure's current–voltage (I-V) behavior under reverse bias conditions was carried out using the Tektronix 4200A-SCS parameter analyzer and probe station. Initially, two probes were linked to the SMU-1 (Source Measurement Unit—1) and GND (Ground) of the parameter analyzer. These connections were then directed to the cathode and anode terminals of the sample, respectively. The Clarius software associated with the parameter analyzer streamlined the configuration of voltage–current measurement steps. The reverse voltage magnitude ($|V_R|$) was systematically varied from 0 to 19.5 V in increments of 1.5 V, and the corresponding I_0 values were measured and recorded. The experimentally obtained I_0 versus V_R graphs for the ten-element lo-hi-lo HEM-ATT sample were then graphed, as illustrated in Figure 5. Moreover, Figure 5 presents the I-V characteristics of the ten-element lo-hi-lo HEM-ATT structure derived from DC simulation, where the current density values (J_0) underwent multiplication by the cross-sectional area to ascertain the corresponding current (I_0) values. Figure 5 reveals a noteworthy consistency between the I-V characteristics obtained from experimental measurements and DC simulation, affirming the validity of the simulation model employed in this study. The breakdown voltage obtained from DC simulation was 16.61 V, closely aligned with the experimentally measured breakdown voltage of 17.35 V, thereby validating the simulated value. Examining the I-V characteristics of the ten-element lo-hi-lo HEM-ATT structure depicted in Figure 5 reveals an interesting observation. The breakdown voltage of the entire structure remains relatively unchanged when compared to the previously reported single-element lo-hi-lo HEM-ATT device [53]. However, there is a notable increase in the current at each voltage point, nearly by a factor of ten. This outcome is expected, given that in the proposed multi-element structure, all HEM-ATT devices are effectively connected in parallel. As a result, the voltage across the diode stays constant ($V_{D(N)} = V_{D(1)}$), but the

current through it experiences a significant increase ($I_{D(N)} \approx N \times I_{D(1)}$).

B. CHARACTERISTICS OF THE COUPLING CIRCUIT

In Figure 6 (a), variations in the guided wavelength (λ_g) through coupling circuits and the free space wavelength (λ_0) are presented concerning the design frequency of the source. Within the frequency range of 0.923 to 1.066 THz, the guided wavelengths (121.853 – 105.507 μm) consistently exhibit shorter values than the corresponding free space wavelengths (325.027 – 281.426 μm), a result of the effective dielectric constant of the insulating layer surpassing unity. Figure 6 (b) indicates that the maximum operating frequency of the designed coupling circuits ($f_C^{(max)}$) significantly surpasses the operating frequency of the source (f_p), ensuring effective coupling between adjacent diodes. The effective dielectric constant ($\varepsilon_r^{(eff)}$) of the Si$_3$N$_4$ insulator layer is observed to decrease, and the phase velocity of the wave (v_{ph}) increases with the source's operating frequency, as depicted in Figures 7 (a) and (b) respectively. Throughout different frequencies of operation, the effective dielectric constant consistently remains smaller than the actual dielectric constant (ε_r) of the insulating layer (Si$_3$N$_4$) due to fringing fields arising from the edge effect associated with the nanostrip lines. In Figure 8 (a), the equivalent resistance of the coupling circuits ($R_L^{(i,i+1)}$) increases from 12.275 to 13.372 mΩ with the rise in operating frequency from 0.923 to 1.066 THz. Concurrently, the equivalent capacitance ($C^{(i,i+1)}$) and inductance ($L^{(i,i+1)}$) decrease from 11.079 to 8.874 pF and from 2.684 to 2.512 fH, respectively, within the same frequency increment. Figure 8 (b) demonstrates an increase in the magnitude of the coupling parameter from 19.822 to 21.491 mΩ with an increase in operating frequency from 0.923 to 1.066 THz. The phase angle of the coupling parameter remains consistently at zero for all operating frequencies.

C. THZ CHARACTERISTICS

If the elements of the source are not identical, the frequency of oscillation of different HEM-ATT-elements will deviate from each other, leading to a structural mismatch following fabrication. To simulate this structural mismatch, the length of the active layer of each element is varied randomly by an amount $\delta l = \left(L_d^{(prac)} - L_d \right)$, where L_d represents the design-length (specified in Table 1) and $L_d^{(prac)}$ is the active region length after fabrication. The parameter δl is denoted as the length-mismatch-parameter, characterized as a

random-variable with a probability density function which follows normal distribution with zero mean value. It is typically expressed as a percentage, $\Delta l = (\delta L / L_d) \times 100\%$.

The simulations were executed by introducing varying levels of the mismatch parameter, spanning from 0 to ±10%. Multiple trials were conducted to assess the impact of length-mismatch on the high-frequency and noise characteristics of the 10-element HEM-ATT source, both in the presence and absence of mutual injection locking. Figures 9 (a) and (b) illustrate the normalized power spectral densities (PSDs) of the 10-element 1.0 THz HEM-ATT source without ($\kappa^{(i,i+1)} \to \infty$) and with ($\kappa^{(i,i+1)} < \infty$) mutual injection locking, respectively, for $\Delta l = 0\%$. Figure 9(c) presents the same for $-10\% \leq \Delta l \leq +10\%$. Observations from Figures 9(a) and (b) indicate that the PSD of the source is highly narrowband around 1.0 THz, suggesting that injection locking is unnecessary in an ideal case without mismatch. However, in Figure 9 (c), the PSD reveals multiple peaks when a mismatch is present ($|\Delta l| = 10\%$), indicating the generation of several local harmonics around 1.0 THz. Notably, Figure 9 (c) emphasizes that mutual injection locking compels all elements to oscillate at a single frequency near 1.0 THz, even when substantial mismatch conditions are present ($|\Delta l| = 10\%$).

The 3-dB bandwidth ($BW_p^{(\kappa)}$) of the source exhibits a rapid increase with the augmentation of the mismatch amount ($|\Delta l|$) in the absence of mutual injection locking. Conversely, the same 3-dB bandwidth is nearly constant in a mutually injection-locked source, despite variations in $|\Delta l|$. In Figure 9(d), it is evident that in the 1.0 THz source, the bandwidth increases from 18.32 to 128.91 GHz as $|\Delta l|$ varies from 0% to 10% in absence of mutual injection locking. In contrast, for the mutually injection locked 1.0 THz source, the bandwidth variations are observed to be within the range of 18.32 to 24.87 GHz for the same $|\Delta l|$ variation. Importantly, Figure 9 (d) highlights that the 3-dB bandwidth of the source is substantially reduced when mutual injection locking is applied, as it enforces the sources to oscillate at a single frequency.

Mutual injection locking results in a slight decrease in the magnitudes of negative resistance and capacitive reactance when there is a specific level of length-mismatch (in this case, $|\Delta l| = 10\%$). This phenomenon is depicted in Figure 10(a). Consequently, the overall magnitude of the negative resistance of the source decreases, and the high-frequency current redistributes across different source elements. As a consequence of these effects, there is a slight decrease in power output. Figures 10 (b) and (c) illustrate the variations in THz power output and DC-to-

THz conversion efficiency, respectively, for a 10-element HEM-ATT oscillator in absence and in presence of mutual injection locking. These variations are shown concerning bias current, with the length-mismatch varying within the range of $-10\% \leq \Delta l \leq +10\%$. Notably, both power output and efficiency of the source deteriorate, particularly at higher bias current densities, due to the active layer length mismatch.

Figure 11 (a) displays the variations in THz power output with the operating frequency of the source, considering a maximum 10% active layer length mismatch among the elements. The same figure also presents the simulated and experimentally measured power outputs of DDR IMPATT sources based on Si, GaAs, InP, type-IIb diamond, 4H-SiC, and Wurtzite (Wz)-GaN, along with a Schottky barrier (SB) SDR Wz-GaN IMPATT source [47, 68-76]. Importantly, Figure 11 (a) highlights that the power output of the mutually injection locked ten-element HEM-ATT source surpasses that of all the previously mentioned THz sources at 1.0 THz. The DDR 4H-SiC IMPATT source emerges as the closest competitor in terms of THz power output at this frequency. However, the notable advantage of the mutually injection locked 10-element HEM-ATT source lies in its capacity to enhance THz power delivery by increasing the number of elements beyond ten ($N > 10$). Figure 11(b) illustrates the variations in THz power output the source with the number of elements. Noteworthy is the non-linear relationship observed in Figure 11(b): the THz power output of a N-element HEM-ATT source does not vary linearly ($P_{THz(N)} \neq N \times P_{THz(1)}$) with the with the number of elements. Instead, the THz power output experiences deterioration for higher values of N, particularly for $N \geq 4$. This decline is attributed to the influences of coupling circuits and the active layer length mismatch among the numerous elements.

D. NOISE CHARACTERISTICS

The noise simulation for the 10-element HEM-ATT source under mutual injection locking was also conducted at small-signal conditions [65]. The plot in Figure 12 displays the noise measure (NM) versus frequency, demonstrating that the combined influence of active layer mismatch and mutual injection locking induces a slight change in the noise measure, particularly at higher operating frequencies. The positive feedback of avalanche noise current from one element to the adjacent element, and its subsequent multiplication in the avalanche region of the second element and so forth, leads to an overall increase in noise power. The noise simulation for the mutually injection-

locked ten-element HEM-ATT source reveals that these sources exhibit significantly less noise compared to standalone Schottky-barrier SDR Wz-GaN IMPATT sources. However, the NM of a conventional DDR Wz-GaN IMPATT source is notably smaller than the Schottky-barrier-diode-based sources. Specifically, the noise measure of the mutually injection-locked ten-element HEM-ATT source varies from 11.92 to 13.44 dB at 1.0 THz, while it is observed to be 16.09 dB at 1.0 THz in the vertical Schottky SDR source. Meanwhile, the GaN DDR IMPATT source demonstrated to be the least noisy THz source, with a noise measure of 10.20 dB at 1.0 THz. However, although the noise performance of the vertical DDR Wz-GaN IMPATT source was found to be superior to the mutually injection-locked 10-element HEM-ATT source in terms of noise, its THz power output is significantly smaller (approximately 10 µW at 1.0 THz). Consequently, the vertical DDR Wz-GaN IMPATT diode is not recommended for realizing THz sources. Conversely, the high-power mutually injection-locked ten-element HEM-ATT source, with compatible noise characteristics, emerges as the most suitable candidate for experimentally realizing high-power THz sources.

E. COMPARISON WITH STATE-OF-THE-ART THZ SOURCES

A comparative analysis between a previously proposed THz source [53], various commercially available THz sources operating nearly at 1.0 THz [77-87], and the mutually injection-locked 10-element Schottky barrier HEM-ATT source, has been presented in this section. The Table 2 lists essential specifications such as frequency range of operation, peak output power, and efficiency for THz sources, including single-element HEM-ATT source, backward wave oscillators (BWOs), folded waveguide sources, carcinotrons, high-electron-mobility transistors (HEMTs), quantum cascade lasers (QCLs), planar Schottky barrier diode multipliers, and harmonic oscillator arrays [77-87]. The BWO with a slow wave structure based on corrugated waveguide, developed and tested by Mineo *et al*. in 2012 [79], stands out as the most capable source for THz generation in the frequency range of 0.85–1.03 THz. This device achieved a power output of 200 mW at 0.85–1.03 THz. Conversely, other devices listed in Table 2 exhibit the capability to deliver very small amount of THz power (few µW–mW) with noticeably small efficiency (less than 1.0%) at THz regime. In contrast, the single-element HEM-ATT source demonstrates the ability to deliver reasonably higher THz power (250–300 mW) with larger efficiency (11–25%) at 0.923 – 1.066 THz, where the

bandwidth of oscillation is 0.143 THz. Notably, the Schottky barrier HEM-ATT diodes requires very low operating voltage (< 17 V), while THz BWOs necessitate a smallest cathode voltage in the order of kilovolts (KV). Furthermore, the mutually injection-locked 10-element Schottky barrier 1.0 THz HEM-ATT source surpasses its single-element counterpart [53] in terms of THz power delivery capability. Additionally, the THz power output of the mutually injection-locked multi-element HEM-ATT source can be further increased by expanding the number of elements. As a result, the proposed mutually injection-locked multi-element HEM-ATT source exhibits immense potential to become a more promising and reliable THz source compared to existing ones [77-87].

VII. CONCLUSION

The paper explores the terahertz performance of an AlGaN/GaN 2-DEG based mutually injection-locked multi-element HEM-ATT source. The implementation of a nanostrip patch type planar coupling circuit enables injection locking between the adjacent elements. The study offers a thorough analysis of the integrated power combining technique in the mutually injection locked multi-element HEM-ATT oscillator. Specifically, a 10-element mutually injection locked integrated power combined source is designed for operation at 1.0 THz, and simulation studies are conducted to assess its DC, large-signal, and avalanche noise characteristics. The results indicate the capability of the ten-element HEM-ATT oscillator to deliver 2.27 W peak power with a remarkable 17% DC to THz conversion efficiency at 1.0 THz. The average noise measure of the oscillator is found to be 12.54 dB. Notably, the study verifies the oscillator's ability to generate a narrow-band terahertz wave by introducing various levels of structural mismatch between the elements. Moreover, mutual injection locking between adjacent elements is demonstrated to lead the sources to oscillate at a single frequency, even in the presence of a significantly high level of structural mismatch among the elements. However, it is observed that there is a minor reduction in power output and a slight increase in noise measure for the multi-element HEM-ATT oscillator due to the presence of mutual injection locking between adjacent elements. Furthermore, it is demonstrated that the THz power delivery capacity of the mutually injection locked multi-element HEM-ATT source can be enhanced by increasing the number of elements. The research concludes by comparing the terahertz performance of the mutually injection locked 10-

element HEM-ATT oscillator with other state-of-the-art
THz sources, assessing its potential as an excellent
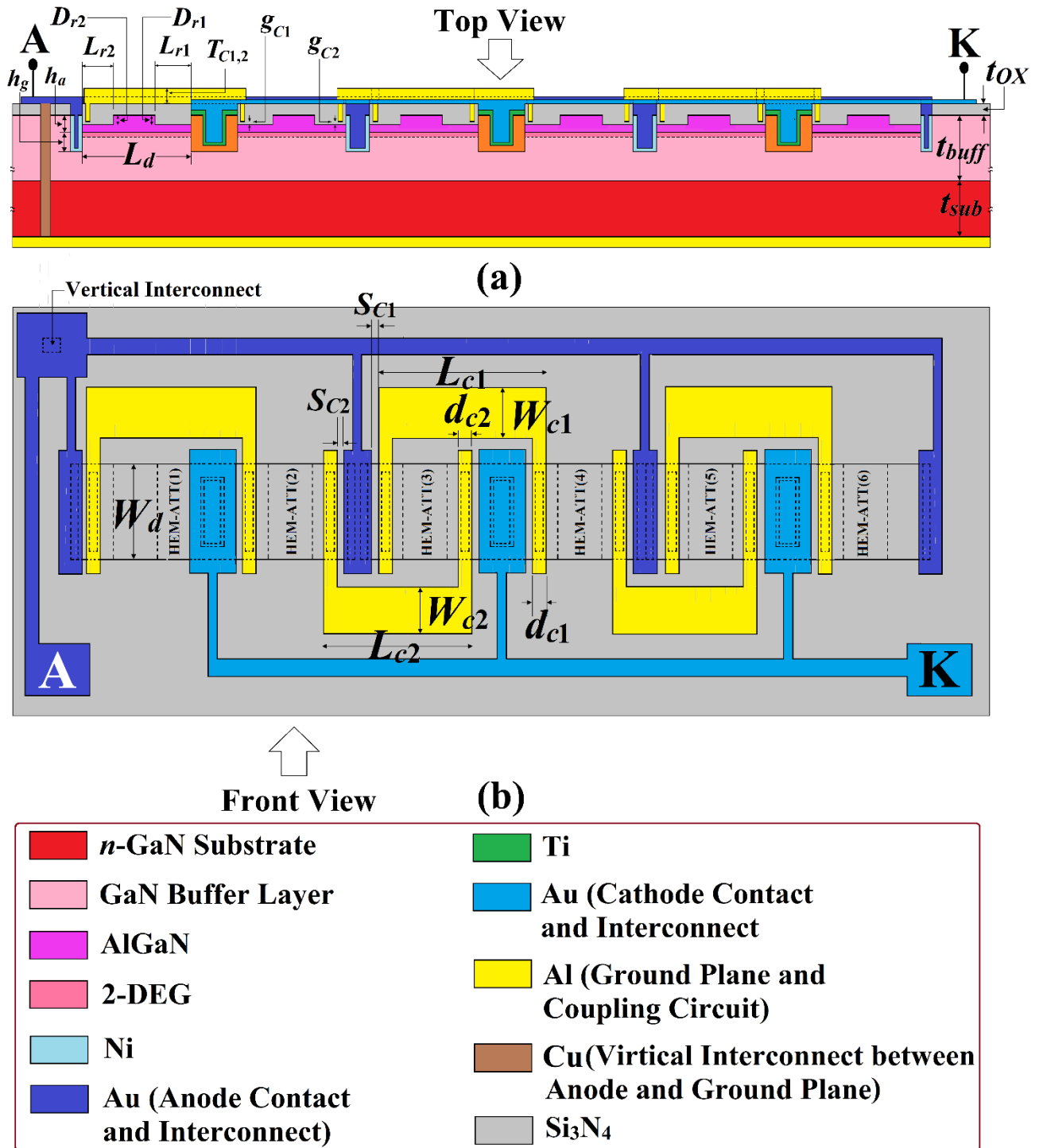integrated THz radiator.

VIII. FIGURES

FIGURE 1. Cross-sectional (a) front and (b) top views of mutually injection locked six-element HEM-ATT oscillator structure.
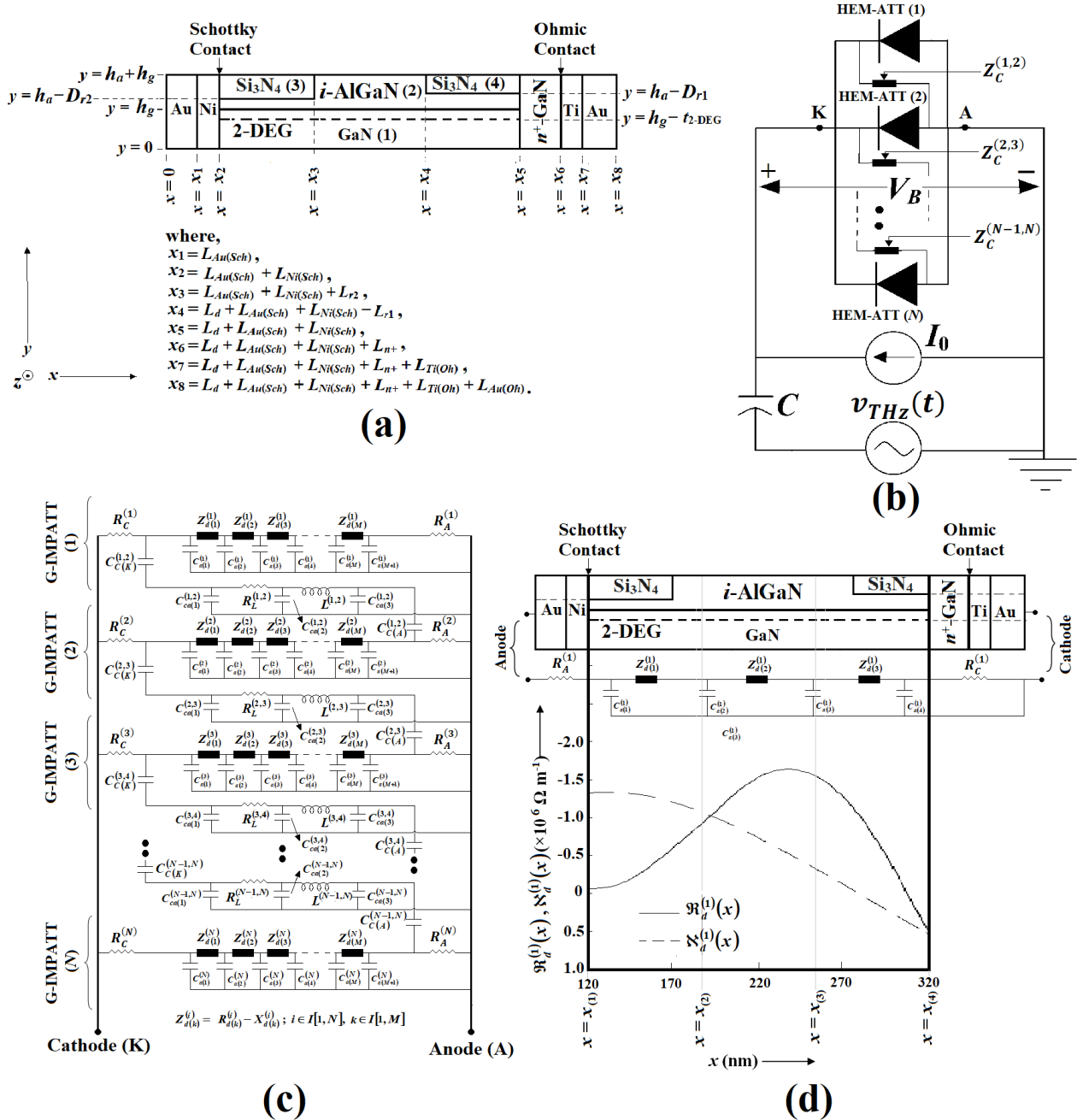
FIGURE 2. (a) 2-D model depicting the lo-hi-lo HEM-ATT structure, (b) external high-frequency equivalent circuit model, (c) equivalent circuit of the mutually injection locked N-element THz HME-ATT source under free oscillating condition, and (d) diagram depicting the approach for computing diode impedance using spatial distributions of diode resistance and reactance per unit length.
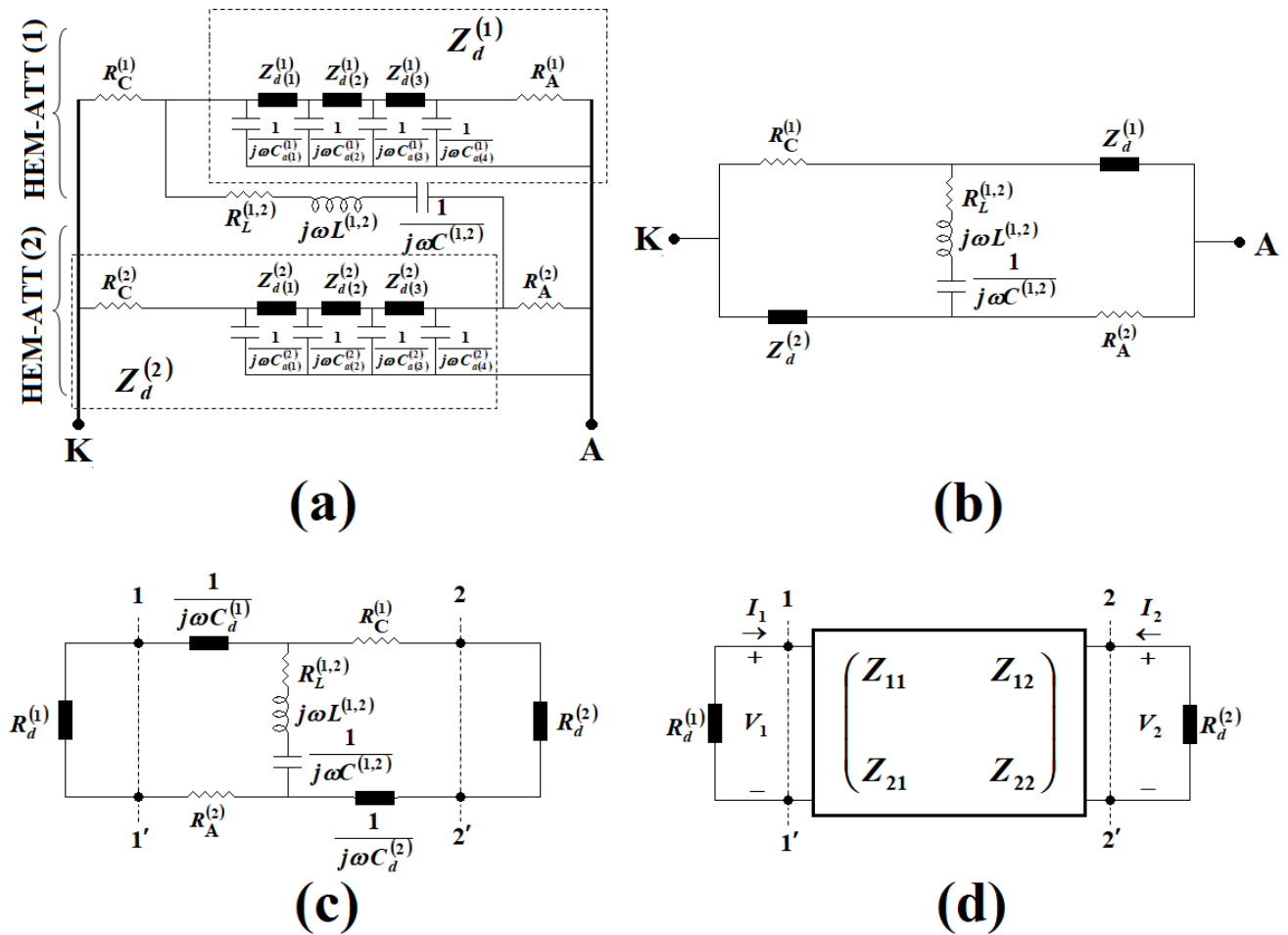
IEEE *Access*
Multidisciplinary ⋮ Rapid Review ⋮ Open Access Journal

FIGURE 3. (a) Reduced equivalent circuit, (b) simplified equivalent circuit, (c) 2-port network model of the mutually injection locked 2-element HEM-ATT oscillator, and (d) Z-parameter equivalent of the 2-port network.
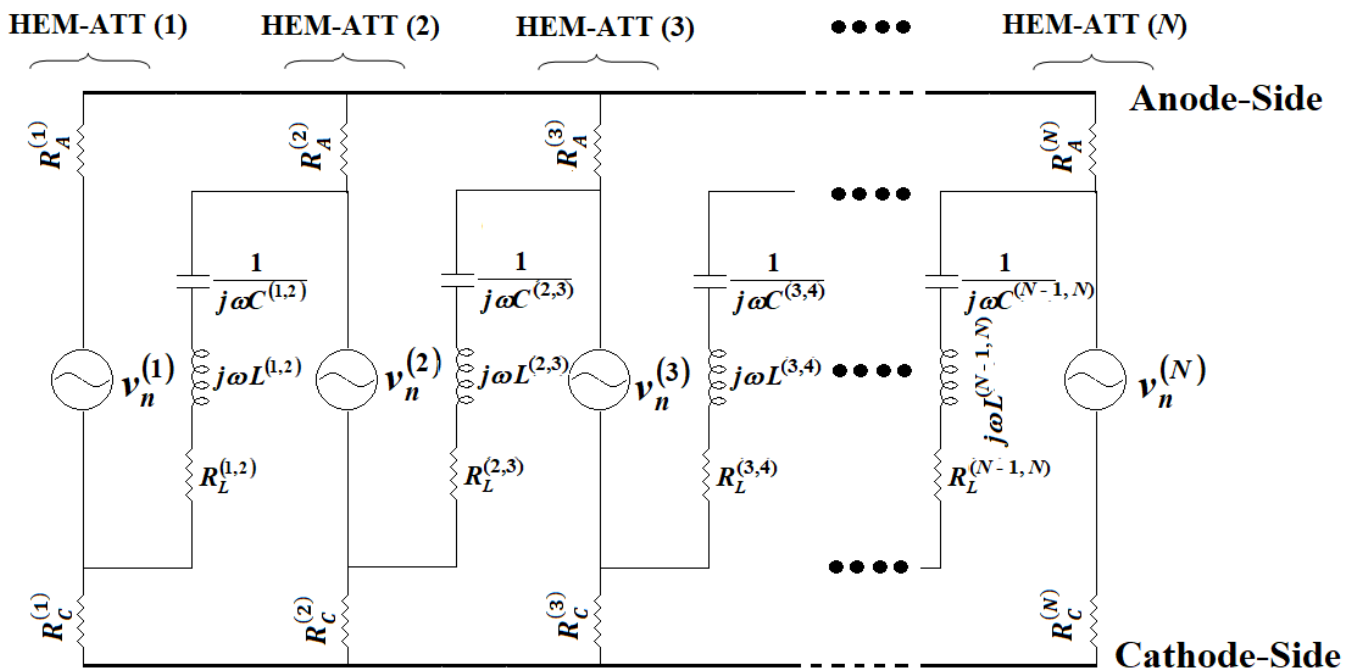

FIGURE 4. Equivalent circuit of mutually injection locked N-element HEM-ATT oscillator for the avalanche noise analysis.
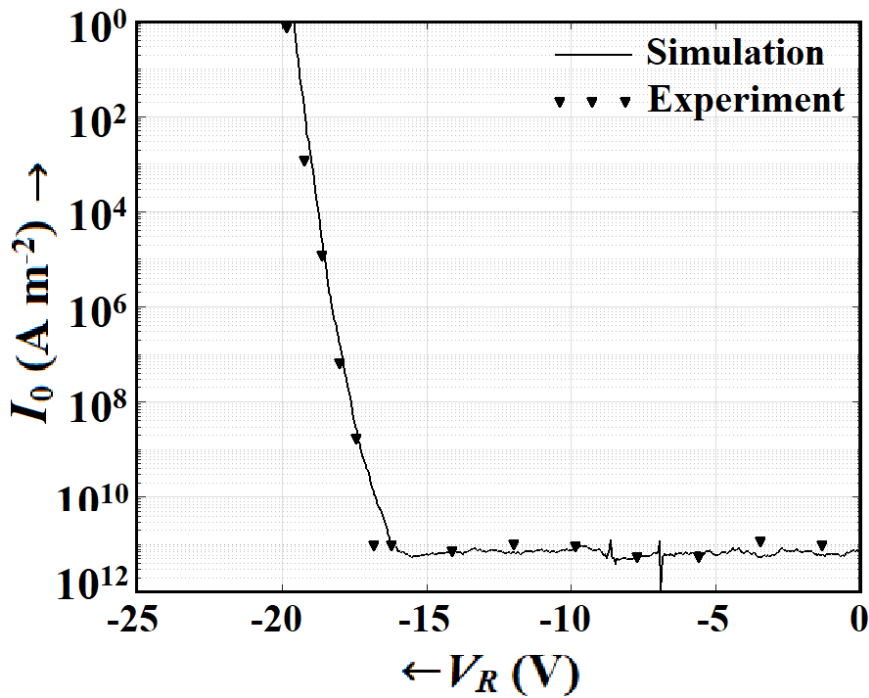
1

IEEE *Access*
Multidisciplinary : Rapid Review : Open Access Journal

FIGURE 5. Reverse bias I-V Characteristics of the ten-element mutually injection locked HEM-ATT oscillator.
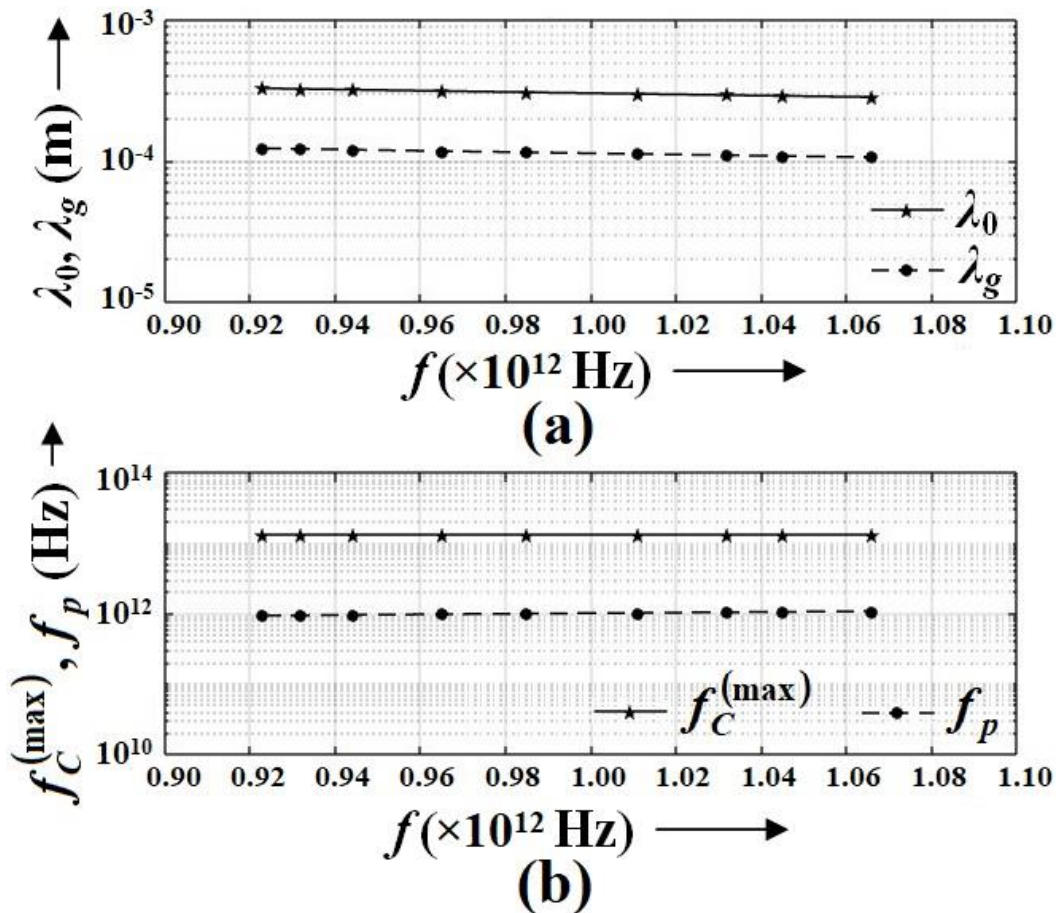

FIGURE 6. Variations of (a) free space wavelength and guided wavelength, and (b) maximum operating frequency of the coupling circuit and the optimum frequency of the source with frequency.
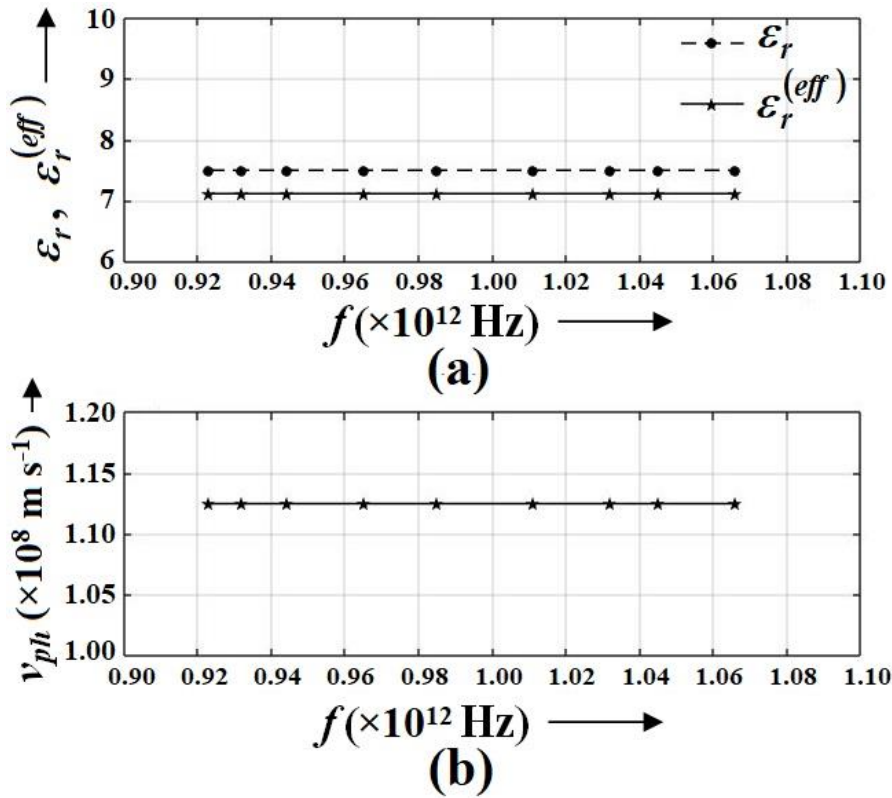
IEEE *Access*

Multidisciplinary : Rapid Review : Open Access Journal

FIGURE 7. Variations of (a) actual and effective dielectric constant of the oxide layer, and (b) phase velocity of the THz wave with frequency.
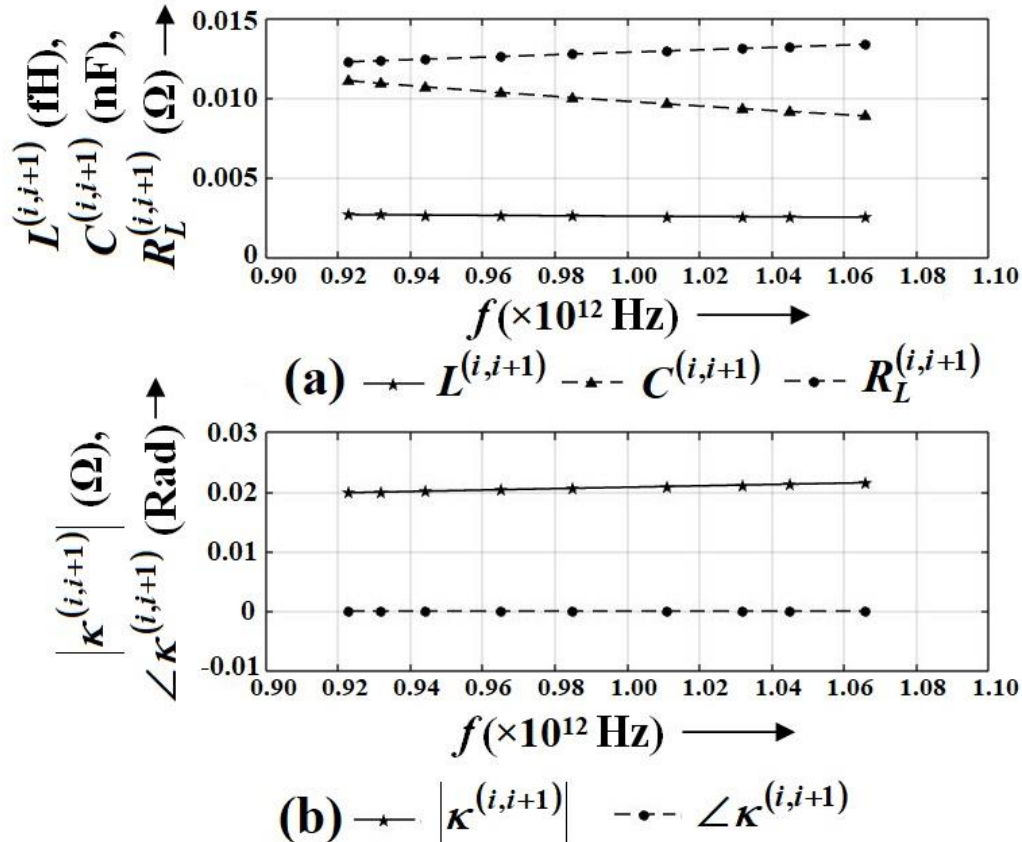

FIGURE 8. Frequency response of the (a) equivalent inductance, capacitance and resistance of the coupling circuit, and (b) magnitude and phase of the coupling parameter.
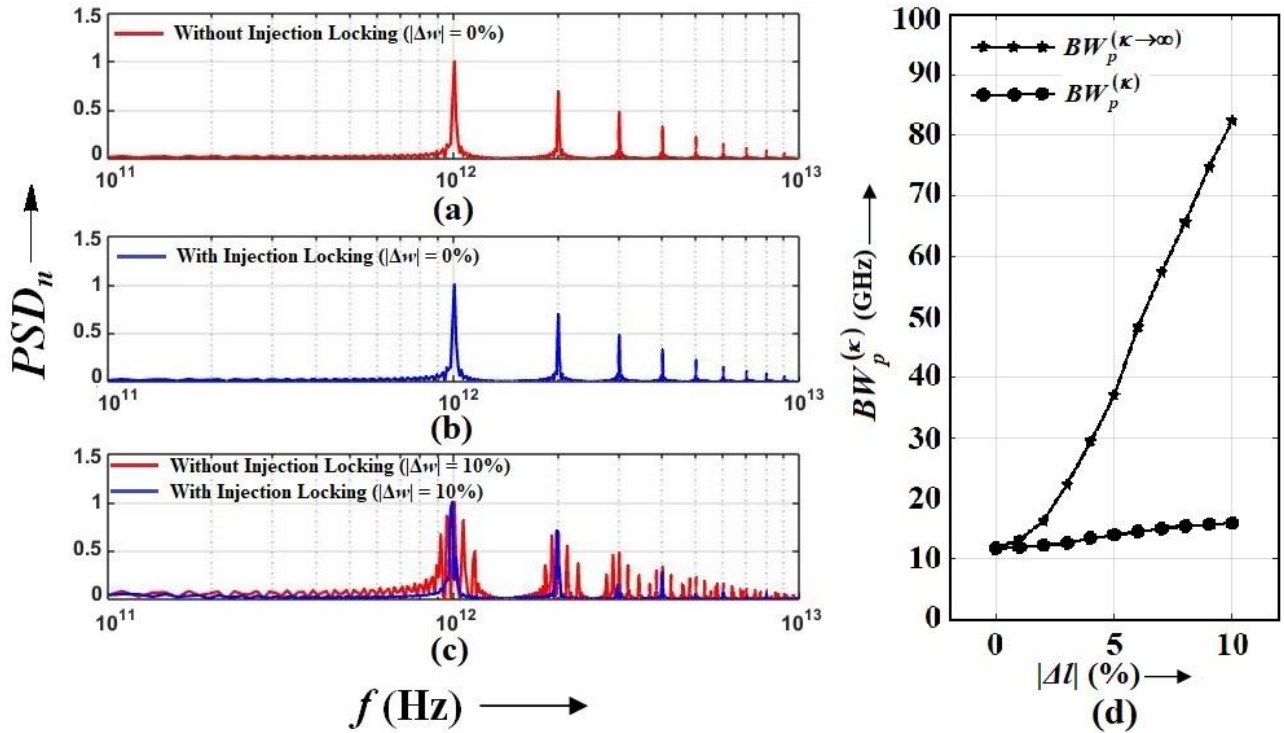
IEEE *Access*

FIGURE 9. Normalized PSD in 10-element 1.0 THz HEM-ATT oscillator versus frequency (a) in absence of and (b) in presence of mutual injection locking by neglecting the length-mismatch, and (c) in absence and in presence of mutual injection locking for length-mismatch varying within the range of −10% ≤ *Δl* ≤ +10%; (d) 3-dB bandwidth of the oscillator in absence and in presence of mutual injection locking, versus length-mismatch parameter.
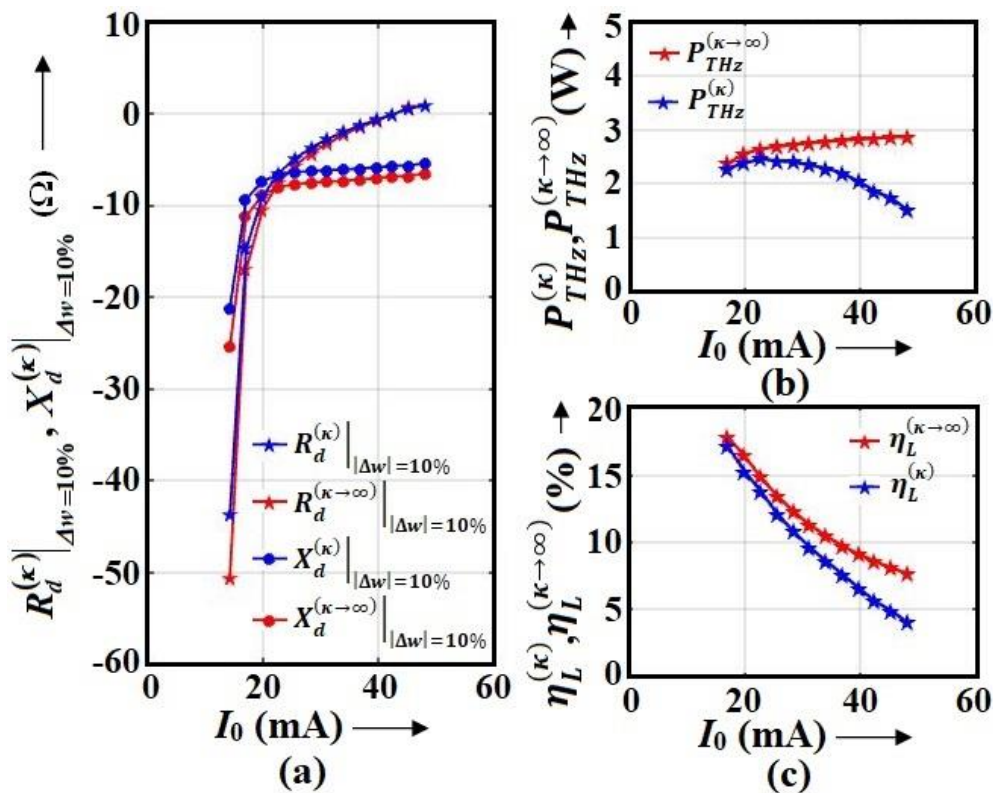

FIGURE 10. (a) Overall resistance and reactance, (b) power output, and (c) conversion efficiency of the 10-element HEM-ATT oscillator in absence and in presence of mutual injection locking, versus bias current for length-mismatch varying within the range of −10% ≤ Δl ≤ +10%.
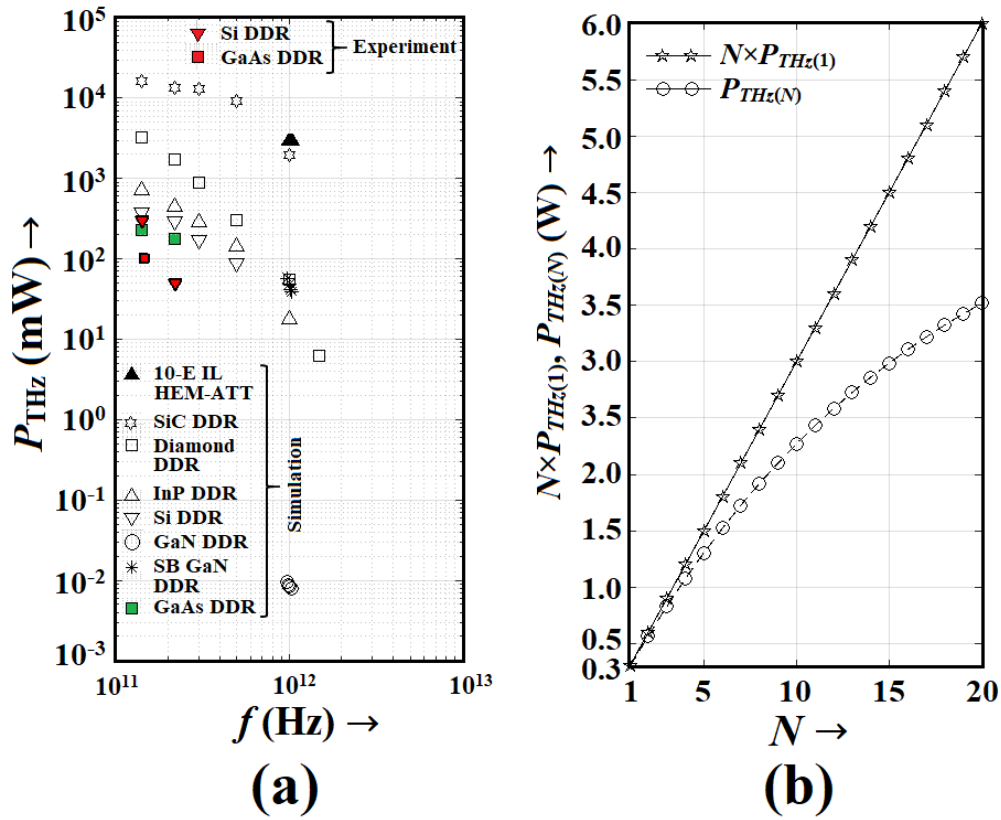
FIGURE 11. Variations of (a) THz power output of ten-element HEM-ATT oscillator and other IMPATT sources with frequency, and (b) THz power output of single or multi-element HEM-ATT oscillator with the number of elements.

FIGURE 12. Noise measure of 10-element HEM-ATT oscillator and other IMPATT sources versus frequency; error bars shows the variations of noise measure due to the combined influence of the length-mismatch varying within the range of −10% ≤ Δl ≤ +10% and mutual injection locking.

IX. TABLES

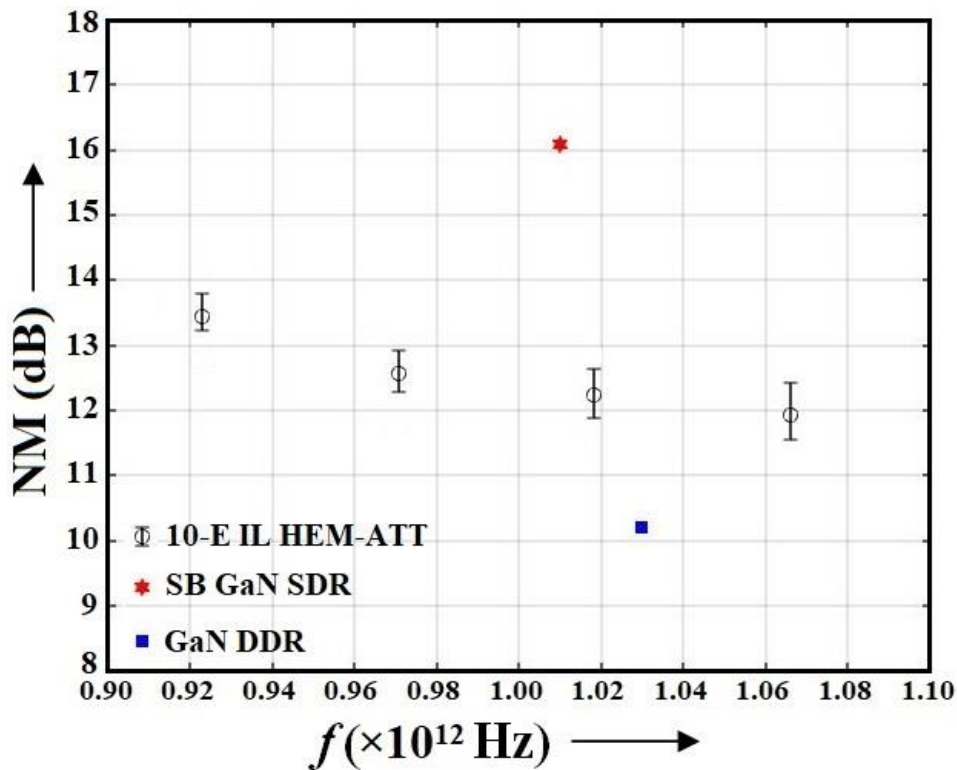| Sl. No.	Parameter Type	Oscillator/Device/Coupling-Circuit	Parameter	Value
1	Design Frequency	Oscillator	f_d (Hz)	1.000×10^{12}
2	Bias Current	Oscillator	J_0 ($\times 10^8$ A m^{-2})	$60.0 - 150.0$
3	Structural (Height)	Device	h_a (nm)	20
4	Structural (Height)	Device	h_g (nm)	20
5	Structural (Height)	Device	t_{sub} (nm)	500
6	Structural (Height)	Device	t_{buff} (nm)	350
7	Structural (Height)	Device	t_{OX} (nm)	100
8	Structural (Length)	Device	L_d (nm)	200
9	Structural (Length)	Device	L_{n+} (nm)	100
10	Structural (Length)	Device	$L_{Ni(Sch)}$ (nm)	30
11	Structural (Length)	Device	$L_{Au(Sch)}$ (nm)	400
12	Structural (Length)	Device	$L_{Ti(Oh)}$ (nm)	30
13	Structural (Length)	Device	$L_{Au(Oh)}$ (nm)	200
14	Structural (Height)	Device	D_{r1} (nm)	10
15	Structural (Length)	Device	L_{r1} (nm)	50
16	Structural (Height)	Device	D_{r2} (nm)	10
17	Structural (Length)	Device	L_{r2} (nm)	50
18	Structural (Width)	Device	W_d (μm)	50
19	Doping	Device	N_{sub} (m^{-3})	1.0×10^{23}
20	Doping	Device	N_{buff} (m^{-3})	1.0×10^{17}
21	Doping	Device	N_{AlGaN} (m^{-3})	1.0×10^{17}
22	Doping	Device	N_{n+} (m^{-3})	2.0×10^{24}
23	Structural (Length)	Coupling-Circuit	L_{C1} (μm)	0.66
24	Structural (Length)	Coupling-Circuit	L_{C2} (μm)	0.66
25	Structural (Length)	Coupling-Circuit	S_{C1} (nm)	10
26	Structural (Length)	Coupling-Circuit	S_{C2} (nm)	10
27	Structural (Length)	Coupling-Circuit	d_{C1} (nm)	20
28	Structural (Length)	Coupling-Circuit	d_{C2} (nm)	20
29	Structural (Height)	Coupling-Circuit	T_{C1} (nm)	100
30	Structural (Height)	Coupling-Circuit	T_{C2} (nm)	100
31	Structural (Height)	Coupling-Circuit	g_{C1} (nm)	5
32	Structural (Height)	Coupling-Circuit	g_{C2} (nm)	5
33	Structural (Width)	Coupling-Circuit	W_{C1} (μm)	6.97
34	Structural (Width)	Coupling-Circuit	W_{C2} (μm)	6.97

TABLE 1: Design parameters of mutually injection locked ten-element (N = 10) HEM-ATT Oscillator.

IEEE Access
Multidisciplinary : Rapid Review : Open Access Journal

Sl. No.	Type of the Source	Important Specifications	Operational Frequency Range (THz)	THz Power Output (W)	DC to THz Conversion Efficiency (%)	Citation
1	Mutually injection locked ten-element HEM-ATT source	Mutually injection locked multi-element ATT source based on AlGaN/GaN 2-DEG	0.923–1.066	1.49 – 2.27	3.93 – 17.04	Present Work
2	Schottky barrier lateral HEM-ATT source	Single-element ATT source based on AlGaN/GaN 2-DEG	0.923–1.066	0.25 – 0.30	11 – 25	[53]
3	Carcinotron	---	0.85	2×10^{-3}	---	[77]
4	Folded waveguide source	---	0.65	59×10^{-3}	---	[78]
5	Backward wave oscillator	Narrow corrugated waveguide as slow wave structure	0.85–1.03	0.20	---	[79]
6	Backward wave oscillator	Vane circuit using 20 mA of current at 7.1 KV, made by milling	0.80–0.96	2.0×10^{-3}	<1.0	[80]
7	Backward wave oscillator	6 KV, 60 A, 15 kg BWO, water-cooled	1.03–1.25	0.5×10^{-3}– 2.0×10^{-3}	<1.0	[81]
8	Quantum cascade laser (QCL)	Monolithic THz source comprises 13.7 QCL coupled with a high-resistivity Si lens	0.60–6.00	0.2×10^{-3}	---	[82]
9	Quantum cascade laser (QCL)	Electrically pumped monolithic source based on long-wavelength dual-upper-state active region	1.03	1.8×10^{-5}	---	[83]
10	Quantum cascade laser (QCL)	Electrically pumped monolithic semiconductor source with intra-cavity non-linear frequency mixing	1.2–5.9	2.87×10^{-3} at 1.5 THz (at 110 K)	<1.0	[84]
11	High-electron-mobility transistor (HEMT)	Tunable room temperature source utilizes the two-dimensional plasma insability in GaN HEMTs	0.75–2.2	0.15×10^{-6}	<1.0	[85]
12	Planner Schottky diode multipliers	---	1.75–2.0	0.40×10^{-4}	<1.0	[86]
13	Harmonic oscillator array	Si-based fully scalable coherent harmonic oscillator array	1.01	0.81×10^{-4}	0.73×10^{-4}	[87]

TABLE 2. Performance comparison between the mutually injection locked ten-element 1.0 THz HEM-ATT oscillator and some state-of-the-art THz sources.

REFERENCES

1. Martyniuk P, Antoszewski J, Martyniuk M, Faraone L, Rogalski A. New concepts in infrared photodetector designs. *Appl. Phys. Rev*. 2014; 1: 041102.

2. Siegel PH. THz Instruments for Space. *IEEE Transactions on Antenna and Propagation* 2007; 55: 2957-2965.

3. Grischkowsky D, Keiding S, Exter M, Fattinger C. Far-infrared time-domain spectroscopy with terahertz beams of dielectrics and semiconductors. *J. Opt. Soc. Am. B*. 1990; 7: 2006-2015.

4. Debus C, Bolivar PH. Frequency selective surfaces for high sensitivity terahertz sensing. *Appl. Phys. Lett*. 2007; 91: 184102.

5. Yasui T, Yasuda T, Sawanaka K, Araki T. Terahertz paintmeter for noncontact monitoring of thickness and drying progress in paint film. *Appl. Opt*. 2005; 44: 6849-6856.

6. Stoik CD, Bohn MJ, Blackshire JL. Nondestructive evaluation of aircraft composites using transmissive terahertz time domain spectroscopy. *Opt. Express*. 2008; 16: 17039-17051.

7. Jördens C, Koch M. Detection of foreign bodies in chocolate with pulsed terahertz spectroscopy. *Opt. Eng*. 2008; 47: 037003.

8. Fitzgerald AJ, Cole BE, Taday PF. Nondestructive analysis of tablet coating thicknesses using terahertz pulsed imaging. *J. Pharm. Sci*. 2005; 94: 177-183.

9. Ward J, Schlecht E, Chattopadhyay G, Maestrini A, Gill J, Maiwald F, Javadi H, Mehdi I. Capability of THz Sources based on Schotiky diode frequency multiplier chains. *IEEE MTT-S Digest*. 2004; 1: 1587-1590.

10. Heyminck S, Güsten R, Graf U, Stutzki J, Hartogh P, Hübers HW, Ricken O, and Klein B. GREAT: ready for early science aboard SOFIA, *Proc. 20th Intl. Symp. Space THz Techn., Charlottesville, VA*. 2009; pp. 315-317.

11. Crowe TW, Hesler JL, Retzloff SA, Pouzou C, Schoenthal GS. Solid State LO Sources for Greater than 2 THz, *2011 ISSTT Digest, 22nd Symposium on Space Terahertz Technology, Tucson Arizona, USA*. 2011; pp. 1-4.

12. Crowe TW, Hesler JL, Retzloff SA, Pouzou C, Schoenthal GS. Multiplier based sources for frequencies above 2 THz, *36th International Conference on Infrared, Millimeter and terahertz Sources (IRMMW-THz)*. 2011; pp. 1-4.

13. Maestrini A, Mehdi I, Siles JV, Ward J, Lin R, Thomas B, Lee C, Gill J, Chattopadhyay G, Schlecht E, Pearson J, Siegel P. First Demonstration of a Tunable Electronic Source in the 2.5 to 2.7 THz Range. *IEEE Trans. Terahertz Science Techn*. 2012; 3: 177-182.

14. Siegel PH. Terahertz technology in biology and medicine. *IEEE Trans. Microw. Theory Tech*. 2004; 52: 2438-2447.

15. M. Tonouchi, Cutting-edge terahertz technology. *Nature Photonics* 2007; 1: 97-105.

16. B. S. Williams, Terahertz quantum-cascade lasers. *Nature Photonics*. 2007; 1: 517-525.

17. Bismuto A, Bidaux Y, Tardy C, Terazzi R, Gresch T, Wolf J, Blaser S, Muller A, Faist J. Extended tuning of mid-IR quantum cascade lasers using integrated resistive heaters. *Optics Express* 2015; 23: 29715-29722.

18. Barate D, Teissier R, Wang Y, Baranov AN, Short wavelength intersubband emission from InAs/AlSb quantum cascade structures. *Applied Physics Letters* 2005; 87: 051103-1-3.

19. Razeghi M, High-performance InP-based mid-IR quantum cascade lasers. *IEEE Journal of Selected Topics in Quantum Electronics* 2009; 15: 941-951.

20. Lai R, Mei X, Deal W, Yoshida W, Kim Y, Liu P, Lee J, Uyeda J, Radisic V, Lange M, Gaier T, Samoska L, Fung A. Sub 50 nm InP HEMT device with f_{max} greater than 1 THz. *in Proc. IEEE Int. Electron Devices Meeting* 2007; pp. 609-612.

21. Deal W, Mei X, Radisic V, Leong K, Sarkozy S, Gorospe B, Lee J, Liu P, Yoshida W, Zhou J, Lange M, Uyeda J, Lai R. Demonstration of a 0.48 THz amplifier module using InP HEMT transistors. *IEEE Microw. Wireless Compon. Lett.* 2010; 20(5): 289-291.

22. Urteaga M, Seo M, Hacker J, Griffith Z, Young A, Pierson R, Rowell P, Skalare A, Rodwell M. InP HBT integrated circuit technology for terahertz frequencies. in Proc. *IEEE Compound Semicond. Integr. Circuit Symp*. 2010; pp. 1-4.

23. Lobisser E, Griffith Z, Jain V, Thibeault B, Rodwell M, Loubychev D, Snyder A, Wu Y, Fastenau J, Liu A. 200-nm InGaAs/InP type-I DHBT employing a dual-sidewall emitter process demonstrating f_{max} >> 800 GHz and f_T = 360 GHz. *in Proc. IEEE Int. Conf. Indium Phosphide Related Materials* 2009; pp. 16-19.

24. Seo M, Urteaga M, Young A, Jain V, Griffith Z, Hacker J, Rowell P, Pierson R, Rodwell M. 300 GHz fixed-frequency and voltage-controlled fundamental oscillators in an InP HBT process. *in IEEE MTT-S Int. Microw. Symp. Dig.* 2010; pp. 272-275.

25. Hacker J, Seo M, Young A, Griffith Z, Urteaga M, Reed T, Rodwell M. THz MMICs based on InP HBT technology. *in IEEE MTT-S Int. Microw. Symp. Dig*. 2010; 1126-1129.

26. Seo M, Urteaga M, Hacker J, Young A, Griffith Z, Jain V, Pierson R, Rowell P, Skalare A, Peralta A, Lin R, Pukala D, Rodwell M, InP HBT IC technology for terahertz frequencies: Fundemental oscillators up to 0.57 THz. *IEEE Journal of Solid-State Circuits*. 2011; 46(10): 2203-2214.

27. Kitagawa S, Mizuno M, Saito S, Ogino K, Suzuki S, Asada M. Frequency-tunable resonant-tunneling-diode terahertz oscillators applied to absorbance measurement. *Japanese Journal of Applied Physics* 2017; 56: 058002.

28. Orihashi N, Hattori S, Suzuki S, Asada M. Experimental and theoretical characteristics of sub-terahertz and terahertz oscillators of resonant tunneling diodes integrated with slot antenna. *Japanese Journal of Applied Physics* 2005; 44: 7809-7811.

29. Suzuki S, Asada M, Teranishi A, Sugiyama H, Yokoyama H. Fundamental oscillation of resonant tunneling diodes avobe 1 THz at room temperature. *Applied Physics Letters* 2010; 97: 242102-1-3.

30. Asada M, Suzuki S. Theoretical analysis of coupled oscillator array using resonant tunneling diodes in subterahertz and terahertz range. *Journal of Applied Physics* 2008; 103: 124514.

31. Kurokawa K, Injection locking of microwave solid-state oscillators. *Proceedings of IEEE* 1973; 61: 1386-1410.

32. Xu KY, Li J, Xiong JW, Wang G. Mutual phase-locking of planar nano-oscillators. *AIP Advances* 2014; 4: 067108-1-8.

33. R. Adler, "A study of locking phenomena in oscillators," Proceedings of the IRE, vol. 34, issue 6, pp. 351-357, 1946.

34. Y. Fukatsu, and H. Kato, "Frequency conversion with gain through sideband locking of an IMPATT diode oscillation," Proceedings of the IEEE, vol. 57, issue 3, pp. 342-343, 1969.

35. C.H. Chien, and G.C. Dalman, "Subharmonically injected phase-locked IMPATT-oscillator experiments," Electronics Letters, vol. 6, issue 8, pp. 240-241, 1970.

36. M. S. Gupta, "A nonlinear equivalent circuit for IMPATT diodes," Solid-State Electronics, vol. 19, issue 1, pp. 23-26, 1976.

37. H. Okamoto, and M. Ikeda, "Injection Locking of an IMPATT Diode Oscillator by Using a Low-Frequency Signal Parametric Injection Locking," 1977 IEEE MTT-S International Microwave Symposium Digest, 21-23 June 1977, DOI: 10.1109/MWSYM.1977.1124416.

38. J. R. Forrest, and A. J. Seeds, "Optical injection locking of IMPATT oscillators," Electronics Letters, vol. 14, pp. 626-627,1978, DOI: 10.1049/el:19780421.

39. H. W. Yen, "Optical injection locking of Si IMPATT oscillators," Appl. Phys. Lett., vol. 36, issue 8, pp. 680–683, 1980.

40. E. M. Gershenzon, A. A. Levites, and L. A. Plokhova, and A. I. Smetanin, "Injection locking of high-power IMPATT oscillators," Radiotekhnika i Elektronika, vol. 29, pp. 2179-2185, 1984.

41. D. Elad, S. Uzan, A. Nahoum, Z. Nativ, E. Friedler, "W-band injection locked pulsed IMPATT source," 17th Convention of Electrical and Electronics Engineers in Israel, 05-07 March 1991, DOI: 10.1109/EEIS.1991.217690.

42. N. M. Kondratiev, V. E. Lobanov, A. E. Shitikov, R. R. Galiev, D. A. Chermoshentsev, N. Yu. Dmitriev, A. N. Danilin, E. A. Lonshakov, K. N. Min'kov, D. M. Sokol, S. J. Cordette, Y.-H. Luo, W. Liang, J. Liu, and I. A. Bilenko, "Recent advances in laser self-injection locking to high-Q microresonators," Topical Review, vol. 18, Art. no. 21305, Mar. 2023, doi: 10.1038/s41377-023-01005-8.

43. X. Liu, J. Hu, Q. Bian, S. Yi, Y. Ma, J. Shi, Z. Li, J. Zhang, N. Chi, and C. Shen, "Recent Advances in Optical Injection Locking for Visible Light Communication Applications," Photonics, vol. 10, no. 3, Art. no. 291, Mar. 2023, doi: 10.3390/photonics10030291.

44. X. Liu and H. C. Luong, "Injection-Locking Techniques for CMOS Millimeter-Wave and Terahertz Signal Generation," IEEE Transactions on Circuits and Systems II: Express Briefs, vol. 69, no. 7, pp. 3037-3043, Jul. 2022, doi: 10.1109/TCSII.2022.3176410.

45. N. M. Kondratiev, V. E. Lobanov, A. E. Shitikov, R. R. Galiev, D. A. Chermoshentsev, et al., "Recent advances in laser self-injection locking to high-Q microresonators," Frontiers of Physics, vol. 18, no. 2, Art. no. 21305, Mar. 2023, doi: 10.1007/s11467-022-1245-3.

46. Acharyya, A.; and Banerjee, J. P. Potentiality of IMPATT devices as terahertz source: An avalanche response time-based approach to determine the upper cut-off frequency limits. IETE J. Res. 2013, 59, 118–127.

47. Acharyya, A.; and Banerjee, J. P. Prospects of IMPATT devices based on wide bandgap semiconductors as potential terahertz sources. Appl.Nanosci. 2014, 4, 1–14.

48. Horita, M.; Takashima, S.; Tanaka, R.; Matsuyama, H.; Ueno, K.; Edo, M.; Takahashi, T.; Shimizu, H.; and Suda, J. Hall-effect measurements of metalorganic vapor-phase epitaxy-grown p-type homoepitaxial GaN layers with various Mg concentrations. Jpn. J. Appl. Phys. 2017, 56, 031001.

49. Liu, Y. Recent research on ohmic contacts on GaN-based materials. IOP Conf. Series: Materials Science and Engineering 2020, 738, 012007-1-6.

50. Zhang, X. Y.; Yang, L. A.; Yang, W. L.; Li, Y.; Ma, X. H.; and Hao, Y. Improved performance of Ni/GaN Schottky barrier impact ionization avalanche transit time diode with n-type GaN deep level defects. Semiconductor Science and Technology 2020, 36, 025001-1-10.

51. Zhang, X. Y.; Yang, L. A.; Ma, Y.; Liu, Y. C.; Yang, W. L.; Ma, X. H.; and Hao, Y. Noise characteristics of Ni/GaN Schottky barrier IMPATT diode based on polar- and nonpolar-oriented wurtzite GaN for terahertz application. Superlattices and Microstructures 2020, 139, 106405-1-10.

52. Zhang, X. Y.; Yang, L. A.; Hu, X. L.; Yang, W. L.; Liu, Y. C.; Li, Y.; Ma, X. H.; and Hao, Y. Simulation Study of Lateral Schottky Barrier IMPATT Diode Based on AlGaN/GaN 2-DEG for Terahertz Applications. IEEE Transactions on Electron Devices 2022, 69, 1006-1013.

53. Sahanowaj Khan, Aritra Acharyya, Hiroshi Inokawa, Hiroaki Satoh, Arindam Biswas, Rudra Sankar Dhar, Amit Banerjee, and Alexey Y. Seteikin, "Terahertz Radiation from High Electron Mobility Avalanche Transit Time Sources Prospective for Biomedical Spectroscopy," Photonics, MDPI Journal, vol. 10, pp. 1-24, 2023.

54. A. Acharyya, "Terahertz Wave Radiation from Mutually Injection Locked Multi-Element Graphene Nanoribbon Avalanche Transit Time Sources," International Journal of Numerical Modelling: Electronic Networks, Devices and Fields, 2020, DOI: 10.1002/jnm.2768.

55. P. Ramm, D. Bonfert, F. Iberl, A. Klumpp, S. Riedel, S. E. Schulz, R. Wieland, M. Zacher and T. Gessner, "Interchip VIA technology by using copper for vertical system integration," Proc. Advanced Metallization Conference (AMC 2001), eds. A. J. Mckerrow et al. (Material Research Society, Pittsburgh, 2001), Mater. Res. Soc. Proc. V-17, p. 159.

56. Majewski, J.; Miskys, C.; Link, A.; Hermann, M.; Eickhoff, M.; Stutzmann, M.; Bernardini, F.; Fiorentini, V.; Tilak, V.; Schaff, B.; and Eastman, L. F. Pyroelectric properties of Al(In)GaN/GaN hetero and quantum well structures. J. Phys.-Condensed Matter 2002, 14, 3399–3434.

57. Ambacher, O.; Smart, J.; Shealy, J. R.; Weimann, N. G.; Chu, K.; Murphy, M.; Schaff, W. J.; Eastman, L. F.; Dimitrov, R.; Wittmer, L.; Stutzmann, M.; Rieger, W.; and Hilsenbeck, J. Two-dimensional electron gases induced by spontaneous and piezoelectric polarization charges in N and Ga-face AlGaN/GaN heterostructures. J. Appl. Phys. 1999, 85, 3222–3233.

58. Ambacher, O.; Foutz, B.; Smart, J.; Shealy, J. R.; Weimann, N. G.; Chu, K.; Murphy, M.; Sierakowski, A. J.; Schaff, W. J.; Eastman, L. F.; Dimitrov, R.; Mitchell, A.; Stutzmann, M. Two-dimensional electron gases induced by spontaneous and piezoelectric polarization in undoped and doped AlGaN/GaN heterostructures. J. Appl. Phys. 2000, 87, 334–344.

59. Yu, E. T.; Sullivan, G. J.; Asbeck, P. M.; Wang, C. D.; Qiao, D.; and Lau, S. S. Measurement of piezo-electrically induced charge in GaN/AlGaN heterostructure field-effect transistors. Appl. Phys. Lett. 1998, 71, 2794–2796.

60. A. Acharyya, S. Banerjee and J. P. Banerjee, "Influence of Skin Effect on the Series Resistance of Millimeter-Wave of IMPATT Devices," Journal Computational Electronics [USA], Springer, vol. 12, issue 3, pp. 511-525, 2013.

61. Chaffin RJ. High-power TRAPATT oscillators from parallel connected low-cost diodes. IEEE Trans. on Microwave Theory and Techniques 1970; 18: 985-986.

62. M. Ghosh, S. Ghosh, and A. Acharyya, Journal of Computational Electronics 2017, 15(4), 1370.

63. Ghosh M, Ghosh S, Bandyopadhyay PK, Biswas A, Bhattacharjee AK, Acharyya A. Noise Performance of 94 GHz Multiple

Quantum Well Double-Drift Region IMPATT Sources. *Journal of Active and Passive Electronic Devices* 2018; 13(2/3): 19-2075.

64. Banerjee, S.; Acharyya, A.; and Banerjee, J. P. Noise Performance of Heterojunction DDR MITATT Devices Based on Si~Si$_{1-x}$Ge$_x$ at W-Band. *Active and Passive Electronic Components* **2013**, 2013, 1-7.

65. Bandyopadhyay, P. K. ; Biswas, A.; Bhattacharjee, A. K.; and Acharyya, A. Influence of carrier-carrier interactions on the noise performance of millimeter-wave IMPATTs. *IETE Journal of Research* **2019**, 65, 515-522.

66. Kawasaki, S.; Ando, Y.; Deki, M.; Watanabe, H.; Tanaka, A.; Nitta, S.; Honda, Y.; Arai, M.; and Amano, H. Experimental demonstration of GaN IMPATT diode at X-band. *Appl. Phys. Exp.* **2021**, 14, 1-8.

67. Chakraborty, D.; Maity, B.; and Mukherjee, M. Design and development of an AlGaN/GaN heterostructure nano-ATT oscillator: Experimental feasibility studies in THz domain. *Micro Nano Lett.* **2020**, 15, 41–46.

68. Acharyya A, Goswami J, Banerjee S, Banerjee JP. Quantum Corrected Drift-Diffusion Model for Terahertz IMPATTs Based on Different Semiconductors. *Journal of Computational Electronics* 2015; 14: 309-320.

69. Biswas A, Sinha S, Acharyya A, Banerjee A, Pal S, Satoh H, Inokawa H. 1.0 THz GaN IMPATT Source: Effect of Parasitic Series Resistance. *Journal of Infrared, Millimeter and Terahertz Waves* 2018; 39(10): 954-974.

70. Luy JF, Casel A, Behr W, Kasper E. A 90-GHz double-drift IMPATT diode made with Si MBE. *IEEE Trans. Electron Devices* 1987; 34: 1084-1089.

71. Wollitzer M, Buchler J, Schafflr F, Luy JF. D-band Si-IMPATT diodes with 300 mW CW output power at 140 GHz. *Electronic Letters* 1996; 32: 122-123.

72. Midford TA, Bernick RL. Millimeter Wave CW IMPATT diodes and Oscillators. *IEEE Trans. Microwave Theory Tech*. 1979; 27: 483-492.

73. Eisele H. Selective etching technology for 94 GHz, GaAs IMPATT diodes on diamond heat sinks. *Solid State Electronics* 1989; 32(3): 253-257.

74. Tschernitz M, Freyer J. 140 GHz GaAs double-Read IMPATT diodes. *Electronic Letters* 1995; 31(7): 582-583.

75. Adlerstein MG, Chu SLG. GaAs IMPATT diodes for 60 GHz. *IEEE Electron Devices Letter* 1984; 5: 97-98.

76. Eisele H, Chen CC, Munns GO, Haddad GT. The potential of InP IMPATT diodes as high-power millimetre-wave sources: first experimental results. *IEEE MTT-S Int. Microwave Symp. Digest* 1996; 2: 529-532.

77. Guidee; P., and Teyssier; L. A 850 – 1000 GHz backward-wave oscillator for advanced applications. *Society of Photo-Optical Instrumentation Engineers (SPIE) Conference Series*, Instrumentation for Submillimeter Spectroscopy, *Kollberg; E.* (*Editor*), 598, 21 April, 1986, pp. 93-98.

78. Tucek; J., Gallagher; D., Kreischer; K., and Mihailovich; R. A compact, high power, 0.65 THz source. In Proceedings of IEEE International Vacuum Electronics Conference *(IVEC 2008)*, Monterey, CA, USA , 22-24 April, 2008, pp. 16-17.

79. Mineo, M.; and Paoloni, C. Comparioson of THz backward wave oscillators based on corrugated waveguides. *Progress in Electromagnetics Research Letters* **2012**, 30, 163-171.

80. Garcin, P. New technologies used for the 1 THz backward wave oscillator. In Proceedings of the International Electron Devices Meeting Technical Digest, San Francisco, CA, USA, 11-14 December, 1988, pp. 850-853.

81. Sub-mm sources from 178 to 1250 GHz based on BWO (backward wave oscillators), Insight Products Co. Available Online: http://www.insight-product.com/submmbwo3.htm (accessed on 16.02.2023).

82. Fujita, K.; Hayashi, S.; Ito, A.; Dougakiuchi, T.; Hitaka, M.; and Nakanishi, A. Broadly tunable lens-coupled nonlinear quantum cascade lasers in the sub-THz to THz frequency range. *Photonics Research* **2022**, 10, 703-710, DOI: 10.1364/PRJ.443819

83. Hayashi, S.; Ito, A.; Hitaka, M.; and Fujita, K. Room temperature, single-mode 1.0 THz semiconductor source based on long-wavelength infrared quantum-cascade laser. *Appl. Phys. Express* *2020,* 13, 112001, **DOI:** 10.35848/1882-0786/abbb3c

84. Fujita, K.; Hayashi, S.; Ito, A.; and Hitaka, M. Sub-terahertz and terahertz generation in long-wavelength quantum cascade lasers. *Nanophotonics* **2019,** 8, 1-7, DOI:10.1515/nanoph-2019-0238

85. El Fatimy, A.; Suemitsu, T.; Otsuji, T.; Dyakonova, N.; Knap, W.; Meziani, Y.M.; Vandenbrouk, S.; Madjour, K.; Théron, D.; and Gaquiere, Ch.; Prystawko, P.; Skierbiszewski, C. Tunable room temperature Terahertz sources based on two dimensional plasma instability in GaN HEMTs. *Journal of Physics: Conference Series* **2009**, 193, 012072, DOI:10.1088/1742-6596/193/1/012072.

86. Mehdi, I.; Siles, J.V; Lee , C.; and Schlecht, E. THz Diode Technology: Status, Prospects, and Applications. *Proceedings of the IEEE* **2017**, 105, 990-1007.

87. Hu, Z.; Kaynak, M.; and Han, R. High-Power Radiation at 1 THz in Silicon: A Fully Scalable Array Using a Multi-Functional Radiating Mesh Structure. *IEEE Journal of Solid-State Circuits* **2018**, 53, 1313-1327.

Partha Banerjee received the B.Tech degree from University of Calcutta (CU), India, in 2011, and the M.Tech. degree from University of Calcutta (CU), India, in 2013 and currently pursuing the Ph.D degree with the department of Electronics and Communication Engineering, National Institute of Technology – Durgapur (NIT-D), India. He is also working as an Assistant Professor with the Department of Electronics and Communication Engineering, Academy of Technology, Adisaptagram, West Bengal, India. He has published 2 international journal, 3 International Conference papers.

Dr. Aritra Acharyya is currently working at Department of Electronics and Communication Engineering, Cooch Behar Government Engineering College, Harinchawra, Ghughumari, West Bengal, 736170, India, as Assistant Professor. He was born in 1986. He received B.E. and M.Tech. degrees from IIEST, Shibpur, India, and Institute of Radio Physics and Electronics, University of Calcutta, India, in the years 2007 and 2010 respectively. Finally he obtained Ph.D. degree

from Institute of Radio Physics and Electronics, University of Calcutta, in the year 2016. His research interests are high frequency semiconductor devices, nano structures, semiconductor physics, transport phenomena, quantum mechanics, optoelectronics, etc. He has published 92 research papers in peer reviewed national and international journals, 70 research papers in national and international conference proceedings, and several book chapters. He also authored and edited 07 and 05 number of books respectively.

RAJIB DAS received the B.Tech degree from West Bengal University of Technology (WBUT), India, in 2011, and the M.E degree from Jadavpur University (JU), India, in 2013 and currently pursuing the Ph.D degree with the department of Electronics and Communication Engineering, National Institute of Technology – Meghalaya (NIT-M), India. He is also working as an Assistant Professor with the Department of Electronics and Communication Engineering, Cooch Behar Government Engineering College, Harinchawra, West Bengal, India. He has 1 international journal, 1 International Conference and 1 book chapter of international repute. His present research interests include Machine learning (ML), Internet of Things (IoT), Air Pollutions, and SCADA based Control systems.

Arindam Biswas received the M.Tech. degree in radio physics and electronics from the University of Calcutta, India, in 2010, and the Ph.D. degree from NIT Durgapur, in 2013. He was a Postdoctoral Researcher with Pusan National University, South Korea, with the prestigious BK21PLUS Fellowship, South Korea. He was a DST-JSPS Invitation Fellow with RIE, Japan; DST-ASEAN Invitation Fellow with Duy Tan University, Vietnam and Taylors University, Malaysia; Visiting Fellow with the Department of Electrical and Computer Engineering, National University Singapore. He has worked as a specially appointed Associate Professor (Visiting) with the Research Institute of Electronics, Shizuoka University, Japan. He is currently an Associate Professor with the School of Mines and Metallurgy, Kazi Nazrul University, West Bengal, India, where he has been actively engaged in teaching, research, and administration. He has 53 technical articles in different journals and 55 conference proceedings, eight authored books, 18 edited volumes, and ten book chapters of international repute. He has received research grants from different funding agencies, namely, SERB, DST-ASEAN, DST-JSPS, and UGC. He has also received international research grant from the Centre of Biomedical Engineering, Tokyo Medical and Dental University in association with RIE, Shizuoka University, Japan, for four consecutive years, from 2019 to 2023. He has supervised six Ph.D. students till date. His research interests include carrier transport in low dimensional system and electronic devices, non-linear optical communication, THz semiconductor source, the IoT, and optimization. He is a Life Member of the Institute of Engineers (India), MGMI, and a Regular Fellow of the Optical Society of India. He was a reviewer for

reputed journals. He has been selected for the IE (I) Young Engineer Award (2019–2020), the KNU Best Researcher Award (Engineering and Technology) 2021, the KNU Best Faculty Award 2022 (Faculty of Science and Technology), and the Best Paper Award in different international conferences. He has organized and chaired different international conferences in India and abroad.

Prof. Anup Kumar Bhattacharjee is a Professor at Department of Electronics and Communication, National Institute of Technology, Durgapur, West Bengal, 713209, India.

DR. SAURAV MALLIK (Member, IEEE) received the PhD degree from the Department of Computer Science and Engineering, Jadavpur University, Kolkata, India, in 2017, while PhD works were conducted in Machine Intelligence Unit, Indian Statistical Institute, Kolkata, India. He is currently a research scientist in University of Arizona, USA. Previously, we worked as a postdoctoral fellow with Environmental Epigenetics, Harvard T H Chan School of Public Health, Boston, USA. Previously, he also worked as a postdoctoral fellow in Department of School of Biomedical Informatics, University of Texas Health Science Center at Houston, Houston, TX and the Division of Bio-statistics, Department of Public Health Sciences, University of Miami Miller School of Medicine, Miami, FL, USA. He has coauthored more than 136 research articles with a Google H-index of 22. His research interests include computational biology, bioinformatics, data mining, bio-statistics, and pattern recognition. He was the recipient of the Research Associate of Council of Scientific and Industrial Research, MHRD, Government of India, in 2017. He was also the recipient of the Emerging Researcher In Bioinformatics Award from Bioclues BIRD Award steering committee, India, in 2020. He is the editor of many journals. His research interests include machine learning, data mining, soft computing and electronics & communications.

Dr. Haya Alshahrani, currently an Assistant Professor at Princess Nourah Bint Abdulrahman University since 2008, possesses a strong foundation in information security. Her dedication to the field is evident through her educational achievements, including a Ph.D. in Computer and Information Systems Security (2020) from the University of Strathclyde, an MS in Information Systems (2011) from King Saud University, and a BS in Information Systems (2008) from King Khalid University. This journey showcases her commitment to ongoing research and expertise within the critical field of information security.

MOHAMED ABBAS Dr. Mohamed Abbas obtained her BSc in Software Engineering, 2019, Faculty of Computing, Engineering and Media, De Montfort University, Leicester, UK. Her research in technology-related topics for mass communication module projects. Furthermore, she researches computer virus threats and the Y2K bug for the news feature writing module and for the social research

module. Currently, she is a master student in computer science college, King Khalid University, Abha, Saudi Arabia.

BEN OTHMAN SOUFIENE Dr. Ben othman soufiene is an Assistant Professor of computer science at the University of Gabes, Tunisia from 2016 to 2024. He received his Ph.D. degree in computer science from Manouba University in 2016 for his dissertation on "Secure data aggregation in wireless sensor networks. He also holds M.S. degree from the Monastir University in 2012. My research interests focus on the Internet of Medical Things,Wireless Body Sensor Networks,Wireless Networks, Artificial Intelligence, Machine Learning and Big Data.